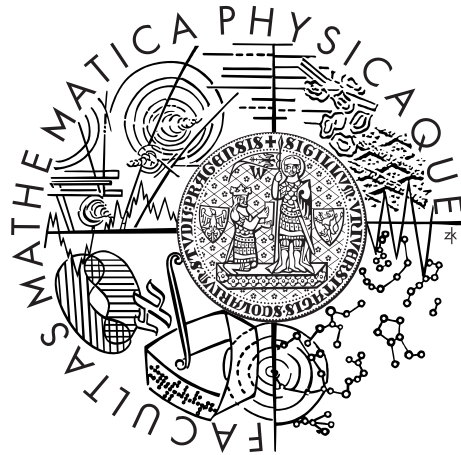


Charles University in Prague
Faculty of Mathematics and Physics

MASTER THESIS



Jana Šmilauerová

Phase transformations and microstructure changes in TIMET LCB alloy

Department of Physics of Materials

Supervisor of the master thesis: Doc. RNDr. Miloš Janeček, CSc.

Study programme: Physics

Specialization: Solid State Physics

Prague 2012

Acknowledgements

In the first place, I would like to thank my supervisor, doc. Miloš Janeček for his support of my work and his guidance and encouragement during my master studies. I am also very grateful to my colleagues from the Department of Physics of Materials for introducing me to the field of materials research. I greatly enjoyed very inspiring and fruitful scientific discussions with them, especially RNDr. Petr Hrcuba and RNDr. Josef Stráský.

I would like to express my gratitude to colleagues from the Department of Condensed Matter Physics, namely doc. Radomír Kužel, Zdeněk Matěj, Ph.D. and Tereza Brunátová, for introducing me to X-ray diffraction analysis, great help with X-ray measurements and for their assistance and numerous suggestions concerning line profile analysis.

I appreciate the support and invaluable comments of Professor Henry J. Rack during my short visit to Clemson University in South Carolina, USA. His extensive knowledge and insight in the physics of phase transformations helped me to understand many different aspects of this subject. I would also like to express my thanks to Herbert Boeckels, who guided me through differential scanning calorimetry measurements and offered many useful scientific suggestions.

This work was financially supported by the Grant Agency of Charles University (grant No. 106-10/251403).

I declare that I carried out this master thesis independently, and only with the cited sources, literature and other professional sources.

I understand that my work relates to the rights and obligations under the Act No. 121/2000 Coll., the Copyright Act, as amended, in particular the fact that the Charles University in Prague has the right to conclude a license agreement on the use of this work as a school work pursuant to Section 60 paragraph 1 of the Copyright Act.

In date

signature

Název práce: Fázové transformace a mikrostrukturní změny ve slitině TIMET LCB

Autor: Jana Šmilauerová

Katedra: Katedra fyziky materiálů

Vedoucí diplomové práce: Doc. RNDr. Miloš Janeček, CSc., Katedra fyziky materiálů

Abstrakt: V předložené práci byly studovány fázové transformace slitiny titanu TIMETAL LCB a jejich vliv na mechanické vlastnosti materiálu. Výchozí stavy byly připraveny pomocí rozpouštěcího žíhání nad teplotou β -přechodu a následně žíhány ve vysokoteplotní oblasti $\alpha + \beta$. Takto bylo dosaženo různých morfologií primární α fáze s konstantním objemovým podílem na hranicích zrn. Takto připravený materiál byl podroben nízkoteplotnímu žíhání při 400 °C, 450 °C a 500 °C. Fázové transformace byly studovány prostřednictvím rentgenové difrakce (XRD), skenovací elektronové mikroskopie (SEM), diferenciální skenovací kalorimetrie (DSC) a měření rezistivity. Mechanické vlastnosti byly vyhodnoceny pomocí měření mikrotvrdomosti a provedením tahových zkoušek. Bylo prokázáno, že po žíhání materiálu při teplotách 400 °C a 450 °C vzniká metastabilní ω fáze, která se po dlouhodobějším žíhání transformuje na drobné precipitáty fáze α . Tyto precipitáty způsobují výrazné zvýšení hodnot mikrotvrdomosti a meze kluzu.

Klíčová slova: Metastabilní β -slitiny titanu, fázové transformace, mikrostrukturní změny, ω fáze

Title: Phase transformations and microstructure changes in TIMET LCB alloy

Author: Jana Šmilauerová

Department: Department of Physics of Materials

Supervisor: Doc. RNDr. Miloš Janeček, CSc., Department of Physics of Materials

Abstract: In the present work, phase transformations in TIMETAL LCB titanium alloy and their influence on mechanical properties were studied. Different initial conditions were prepared by solution treating above β -transus immediately followed by heat treatment in α/β temperature regime. These resulted in different grain boundary α thicknesses and contiguities at a fixed α volume fraction. The subsequent ageing response of this material was studied by low temperature ageing at 400 °C, 450 °C and 500 °C. Phase transformations were studied by X-ray diffraction (XRD), scanning electron microscopy (SEM), differential scanning calorimetry (DSC) and resistivity measurements. Mechanical properties were investigated using microhardness measurements and tensile tests. It has been proved that metastable ω phase is formed during annealing at 400 °C and 450 °C. ω particles further transform to very fine precipitates of α phase when exposed to annealing for longer time periods. These fine precipitates significantly contribute to increase of microhardness and achieving high value of yield stress.

Keywords: Metastable beta Ti alloys, phase transformations, microstructure changes, ω phase

Contents

Acknowledgements	i
1 Introduction	1
2 Background and literature review	2
2.1 Characteristics of titanium	2
2.2 Phases in titanium and its alloys	2
2.2.1 Equilibrium phases	2
2.2.2 Metastable phases	5
2.3 Classification of Ti alloys	7
2.4 Phase transformations	8
2.4.1 $\beta \rightarrow \omega$	8
2.4.2 $\beta \rightarrow \alpha$	9
2.4.3 $\omega \rightarrow \alpha$	10
2.5 Previous works done on phase transformations in LCB	11
3 Experimental procedures	14
3.1 Studied alloy	14
3.2 Heat treatment	15
3.2.1 High temperature annealing	15
3.2.2 Low temperature annealing	15
3.3 Sample preparation	16
3.4 Scanning electron microscopy (SEM)	17
3.5 Microhardness measurements	18
3.6 X-ray diffraction	19
3.7 Differential scanning calorimetry (DSC)	20
3.8 Resistivity measurement	21
3.9 Tensile testing	22
4 Aims and objectives of the work	24
5 Results and Discussion	25
5.1 Microstructure overview of the initial state of the material	25
5.2 Resistivity measurement	26
5.3 Differential scanning calorimetry	29
5.4 Microhardness measurement	30
5.5 X-Ray Diffraction	33
5.6 Scanning electron microscopy	39
5.7 Tensile testing	48
6 Conclusions	50
Bibliography	52
List of Tables	56
List of Figures	57

1. Introduction

Since its discovery in 1791, titanium has had great appeal to scientists and metal designers. Titanium, named after the Titans — children of Uranos and Gaia from Greek mythology — is the fourth most abundant structural metal in the earth's crust after aluminum, iron and magnesium. However, extracting it from its ore minerals rutile (TiO_2) and ilmenite (FeTiO_3) proved to be very difficult, it took more than 100 years to isolate the metal.

Titanium and its alloys are of great interest due to their outstanding properties such as high specific strength, ductility and excellent corrosion resistance. This makes them ideal for use in automotive and aerospace industry as well as for manufacturing biomedical devices and components in chemical processing equipment. The only drawback, which hinders wider use in all above-mentioned fields, is relatively high cost of titanium.

In the last few decades, the importance of β titanium alloys has increased significantly. This present work was conducted on one of the β titanium alloys, TIMETAL LCB (Ti-6.8Mo-4.5Fe-1.5Al in wt.%), where LCB stands for Low Cost Beta. This particular alloy was designed to be used primarily for automotive purposes (e.g. suspension springs) and the aim of its development was to produce a low cost alloy by means of selecting less expensive raw materials (e.g. relatively expensive vanadium was replaced by iron).

This master thesis is divided into six chapters. Chapter 2 characterizes titanium as a metal and provides information on its alloys. Various phases that can be found in titanium alloys and conditions of their occurrence are discussed. In this chapter, the most important phase transformations are also described. Finally, a short literature review of previous studies done on phase transformations in TIMETAL LCB is given. Chapter 3 provides information on the use and basic physical properties of the studied alloy. Furthermore, Chapter 3 focuses on experimental procedures used in this study and describes them thoroughly. Chapter 4 summarizes the aims and objectives of the present work. The next chapter presents the results and discussion of the findings obtained in the research. It deals with phase transformations occurring during ageing treatment of α/β annealed TIMETAL LCB and with their influence on the mechanical properties of the alloy. Finally, Chapter 6 concludes the results of the study and introduces the future investigations.

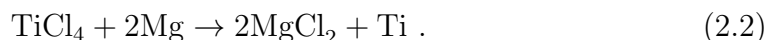
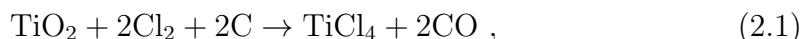
2. Background and literature review

2.1 Characteristics of titanium

Titanium as a chemical element with atomic number 22 belongs to Group 4 of the periodic table of elements. It has a low density and is a strong, lustrous, corrosion-resistant transition metal with a silver color [1]. Its atomic configuration of $[\text{Ar}] 4s^2 3d^2$ enables it to form solid solutions with most substitutional elements with size factor of $\pm 20\%$ [2].

Titanium occurs on Earth naturally in five isotopes, ^{46}Ti through ^{50}Ti , where the isotope ^{48}Ti is the most abundant (73.8%) [1]. Titanium readily reacts with oxygen forming titanium dioxide which is used as a white pigment e.g. in paint, toothpaste or white fireworks.

Titanium is produced commercially from its ores rutile (TiO_2) and ilmenite (FeTiO_3) by the Kroll process, which is a complex and expensive batch procedure. In this process, the oxide is first converted to chloride (TiCl_4) by carbochlorination. The product, titanium tetrachloride, is then purified by fractional distillation and reduced with magnesium in an inert gas atmosphere. The chemical reactions can be written as follows [3]:



The resulting titanium metal is called "titanium sponge" because of its porous and spongy appearance. The sponge can be finally melted in an inert atmosphere to form an ingot.

2.2 Phases in titanium and its alloys

Various phases can be found both in pure titanium and titanium alloys. Their formation depends on several conditions – temperature, pressure, amount of alloying elements or cooling rate. These phases can be generally divided into equilibrium and non-equilibrium (metastable). The equilibrium phase can be defined as a steady state having the lowest Gibbs free energy (G) at given conditions. However, there are also other configurations that correspond to local minima of Gibbs free energy but do not have the lowest possible value of G . Such conditions are called metastable and can be formed by displacive transformations (shearing, shuffling) when high cooling or heating rates are applied. Given favorable conditions and sufficient amount of time, metastable phases will transform into stable ones.

2.2.1 Equilibrium phases

At room temperature and standard pressure, pure titanium crystallizes in a hexagonal close-packed structure (hcp), which is known as the α phase. This

phase has a space group of $P6_3mmc$. Its unit cell is shown in Fig. 2.1a along with the room temperature values of lattice parameters $a = 2.95 \text{ \AA}$ and $c = 4.68 \text{ \AA}$. The c/a ratio of the hexagonal α phase is therefore 1.586, which is smaller than the ideal ratio for hexagonal close-packed structure (1.633). Most densely packed lattice planes and directions are also indicated in Fig. 2.1a. The hexagonal structure of the α phase results in anisotropy of elastic properties of single crystals of α titanium. For example, the elastic modulus varies between 145 GPa for a load parallel to the c -axis and 100 GPa perpendicular to this axis [4]. Similarly, substantial variations in shear modulus can also be observed. The shear modulus ranges from 46 GPa to 34 GPa for stresses applied in $\langle 11\bar{2}1 \rangle$ direction and in (0002) or $\{10\bar{1}0\}$ planes, respectively. These anisotropic properties are obviously much less pronounced in polycrystalline titanium.

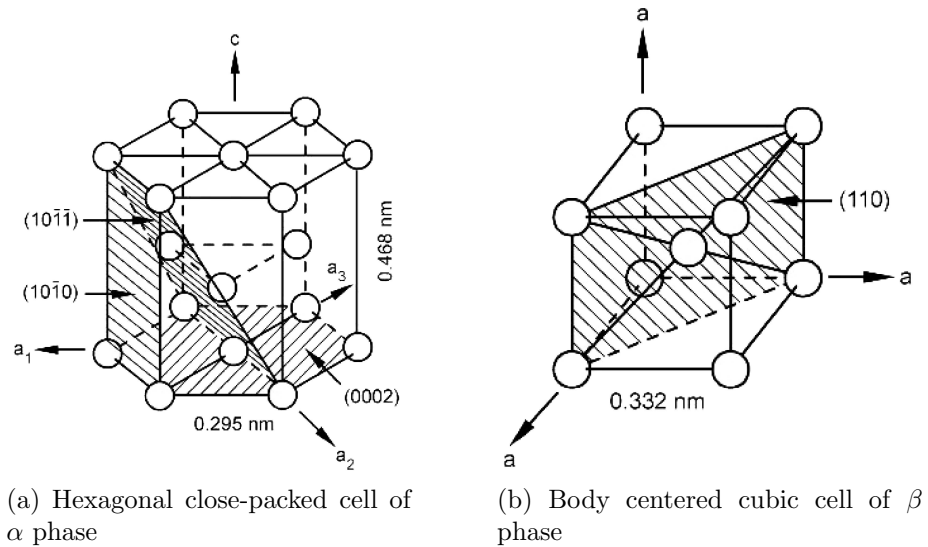


Figure 2.1: Unit cells of Ti [4]

Different slip systems are activated during the plastic deformation of α titanium. Fig 2.2 indicates slip planes and slip directions for hexagonal unit cell. These account for 4 independent slip systems [4]. Thus, according to Von Mises criterion which assumes at least five independent slip systems for a homogeneous plastic deformation in polycrystals, one additional mechanism is required. This is provided either by $\bar{c} + \bar{a}$ slip in the $\langle 11\bar{2}3 \rangle$ direction and in the $\{11\bar{2}2\}$ plane or by twinning [5].

At 882 °C (referred to as the β -transus), pure titanium undergoes an allotropic phase transformation, changing its structure to body centered cubic (bcc) β phase with the lattice parameter of 3.32 Å (see Fig. 2.1b). The body centered cubic structure has two atoms per unit cell and belongs to $Im\bar{3}m$ space group. Due to its more opened structure, it can accommodate higher vibrational entropy. Therefore it is more stable at elevated temperatures than the hexagonal close-packed structure of the α phase.

The elastic modulus of the β phase just above the β -transus temperature is about 58 GPa, whereas the shear modulus is approximately 20 GPa [4]. However, the modulus of elasticity of the β phase in pure titanium cannot be measured at room temperature, as the β phase is not stable.

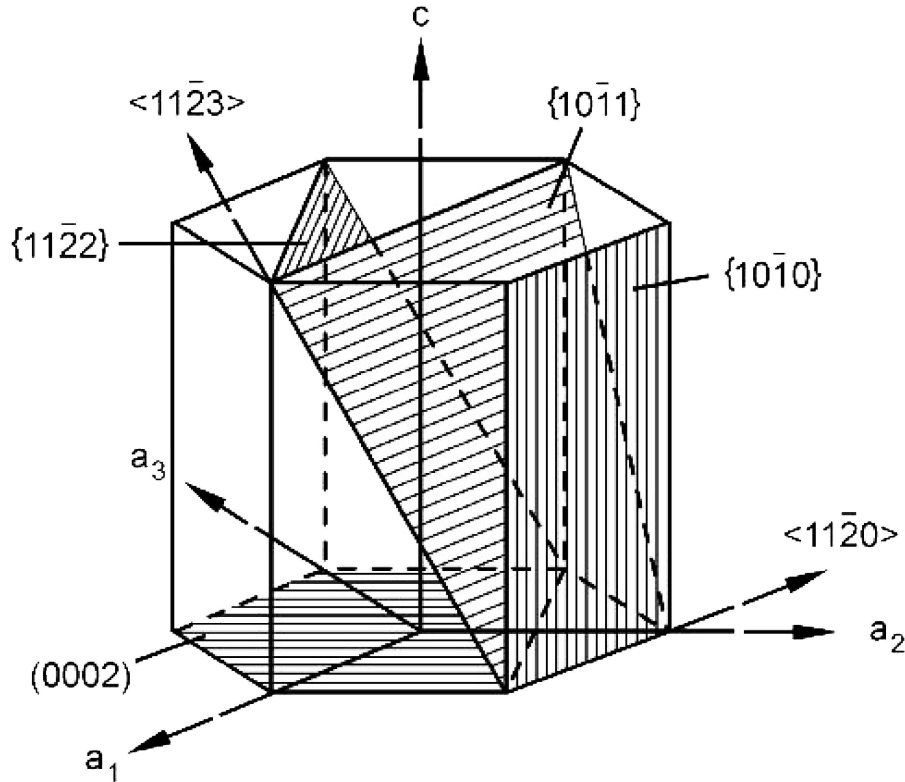


Figure 2.2: Slip planes and directions in the hexagonal α phase [4]

Nevertheless, the stability ranges of the β and α phases can be altered by additions of other metallic elements to obtain a titanium alloy. The main reasons for alloying titanium is to modify the β -transus temperature as well as to introduce a two phase region, where $\alpha + \beta$ coexist. The alloying elements can be divided into three groups according to their influence on the β -transus temperature (see Fig. 2.3) [6]:

- a) α stabilizing,
- b) β stabilizing,
- c) neutral.

α stabilizing elements increase the β -transus temperature with increasing solute content, effectively widening the stability range of the α phase. In this group of alloying additions, Al as a substitutional element and O, N and C as interstitials, are the most common. The most widely used from the above mentioned elements is aluminium, which is the only common metal raising the β -transus temperature having good solubilities both in α and β phases. Other α stabilizing elements include for example B, Ga and Ge but they exhibit much lower solubility than aluminium or oxygen and are not as commonly used.

On the other hand, the β stabilizing elements lower the β -transus temperature and shift the β phase field towards lower temperatures. These alloying additions can be further subdivided into β isomorphous and β eutectoid. Both types are schematically shown in Fig. 2.3. While β isomorphous elements are highly soluble in titanium, even low volume fractions of β eutectoid elements can lead to

formation of intermetallic compounds. The most frequently used β isomorphous elements are V, Mo and Nb. Regarding β eutectoid elements, Cr, Fe and Si are widely used in many titanium alloys, whereas the rest (e.g. Ni, Cu and Mn) has only limited usage.

In order to compare the effects of individual stabilizing elements in titanium alloys, their influence was expressed in terms of molybdenum equivalency depending on the amount of each addition needed to lower the martensitic decomposition of β phase into α phase below room temperature [7]:

$$[\text{Mo}]_{\text{eq.}} = [\text{Mo}] + 0.67 [\text{V}] + 0.44 [\text{W}] + 0.28 [\text{Nb}] + 0.22 [\text{Ta}] + 2.9 [\text{Fe}] + 1.6 [\text{Cr}] + 1.25 [\text{Ni}] + 1.7 [\text{Mn}] + 1.7 [\text{Co}] - 1.0 [\text{Al}] \quad (2.3)$$

The negative constant before aluminium in Equation 2.3 reflects its opposite tendency to stabilize the α phase.

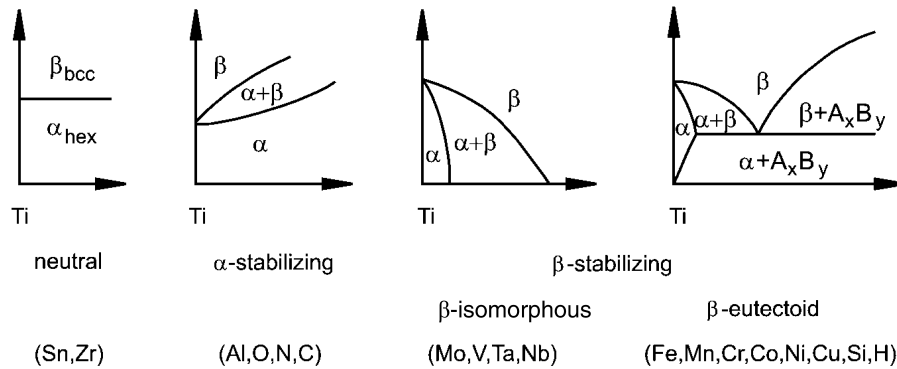


Figure 2.3: Effect of alloying elements on phase diagrams of titanium alloys [5]

The last group of neutral alloying additions (e.g. Zr, Sn) consists of elements which have only minor influence on the β -transus temperature as they tend to lower the β -transus slightly and then again raise it at higher concentrations [4].

Apart from α and β phases, there are some ordered ($B2$, α_2) or intermetallic (γ) phases observed in titanium alloys. These phases are not particularly important for the purpose of this study, therefore, their description is omitted. A detailed description of these phases can be found elsewhere [8], [2].

2.2.2 Metastable phases

One of the most studied metastable phases in titanium alloys is undoubtedly the ω phase. Since its discovery in 1954 by Frost et al. [9] there has been a great interest in investigating the conditions of its precipitation and its influence on mechanical and superconducting properties of titanium alloys. ω phase in titanium alloys forms finely dispersed, submicron precipitates which are coherent with the parent β phase. According to Hickman's review on the formation of ω phase in titanium and zirconium alloys [10] and other literature, there are three main conditions under which the ω phase forms:

1. When the β stabilizer content is high enough to suppress the martensite start temperature below room temperature, ω phase forms upon rapid

quenching. This phase is often referred to as the *athermal* ω in the literature and its formation is a displacive and diffusionless one. It was shown experimentally that this athermal $\beta \rightarrow \omega$ transformation is completely reversible [11] and that even extremely fast quench rates are insufficient to suppress the athermal formation of ω .

2. ω phase can also be formed during isothermal ageing in the temperature range of approximately 100 – 500 °C (the exact temperature range of ω formation varies between different systems depending on the alloying additions to the titanium alloy). This phase is commonly denoted as *isothermal* ω phase. This isothermal transformation is accompanied by rejection of β stabilizing elements from the ω phase, thus the reaction is diffusion-controlled and irreversible. Recently, it has been presumed that rather than ω isothermal and athermal being two completely different phases, isothermal ω is a continuation of athermal ω transformation [12]. The isothermal ω can be distinguished from the athermal type by its slightly larger size and a composition gradient along the β/ω interface. Continued ageing treatment after ω formation results in formation of the equilibrium α phase.
3. Deformation at room temperature has been also shown to cause formation or increase in the amount of the ω phase in some types of titanium alloys (e.g. studies on Ti-Cr alloys by Bagaryatskiy [13] or on Ti-V by Brotzen [14]).

From the crystallographic viewpoint, ω phase is either hexagonal belonging to the $P6/mmm$ space group ([15]) or trigonal having the $P\bar{3}m1$ space group ([16]). The hexagonal symmetry occurs in leaner alloys, while the trigonal symmetry is found in heavily β stabilized alloys [4] or as an incomplete form of the hexagonal ω [17]. For both modifications the lattice parameters are $a = 4.60 \text{ \AA}$ and $c = 2.82 \text{ \AA}$ with resulting c/a ratio of 0.613.

It has been observed that the morphology of the ω phase is ellipsoidal or cuboidal. According to the work done by Blackburn and Williams [18], the shape is related to lattice misfit strain between Ti and alloying addition. When the misfit is small, the particle shape is determined by minimization of the anisotropic surface energy resulting in an ellipsoidal morphology. In higher misfit systems, the cuboidal shape develops due to minimization of the matrix elastic strains. It has been also suggested by the same authors [19] that the degree of misfit between ω particles and β matrix has a significant influence on the ω phase stability. The ω phase is stable for longer times and higher temperatures in low misfit systems than in high misfit systems.

In dilute titanium alloys and pure titanium, a martensitic phase can be formed as a result of rapid quenching or deformation. A martensitic transformation is a cooperative movement of atoms by a diffusionless, shear type process, also known as military transformation [20]. In Fig. 2.4 the region where a martensite can form in titanium alloys is indicated by a dashed line labeled with M_s (martensitic start temperature). With increasing solute content the M_s temperature decreases and thus the martensite is less easily formed.

There are two types of martensitic phase in titanium alloys – hexagonal designated α' and orthorhombic denoted by α'' . In very dilute titanium alloys α'

forms large colonies (massive martensite) which decrease in size with increasing solute content. At a certain amount of alloying additions the colonies degenerate to individual plates having an acicular morphology [21].

When β stabilizer solute content is high enough, metastable ω phase becomes unstable and does not precipitate. Instead, the β phase itself undergoes a phase separation reaction to form β_{lean} and β_{rich} . This reaction occurs either by classical nucleation and growth or by spinodal decomposition depending on kinetics of the reaction [2]. In the literature β_{lean} is often denoted as β' and β_{rich} simply as β (this convention has also been used in Fig. 2.4). It should be noted that both β_{lean} and β_{rich} have the same crystallographic structure as the parent β phase. The only differences are therefore solute content and lattice parameters. β_{lean} forms coherent and uniformly dispersed particles within the β matrix.

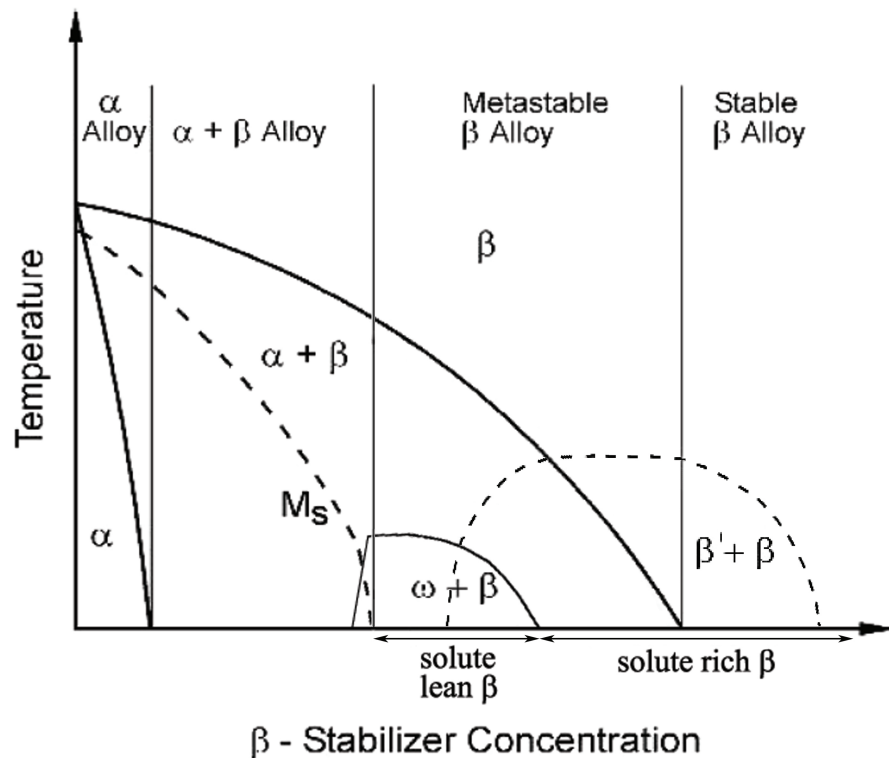


Figure 2.4: Pseudo-binary section through a β isomorphous phase diagram showing important equilibrium and metastable phases as well as the classification of Ti alloys [4]

2.3 Classification of Ti alloys

Titanium alloys are classified into three categories depending on their position in a pseudo-binary section through a β isomorphous phase diagram [4]:

- (a) α alloys,
- (b) $\alpha + \beta$ alloys,
- (c) β alloys.

The three categories are schematically shown in (Fig. 2.4). They differ in volume fractions of different phases and in their morphology.

The first group comprises various grades of commercially pure (CP) titanium and its alloys with only very small amounts of β stabilizers. α alloys can be defined as titanium alloys with no heat treatment response. They exhibit good toughness, good creep resistance and weldability but only moderate strength [22]. They are used for example in some aerospace applications and for sporting goods.

In the β isomorphous phase diagram the group of $\alpha + \beta$ alloys lies in a range from $\alpha/\alpha + \beta$ phase boundary up to the intersection of martensite start (M_s) line with room temperature (Fig. 2.4). Consequently, $\alpha + \beta$ alloys transform martensitically upon rapid quenching from the β phase field. Alloys belonging to this group are heat-treatable and weldable and usually have good balance of strength, ductility and fatigue and fracture properties [4]. One of the best known $\alpha + \beta$ alloy is Ti-6Al-4V (wt. %).

Since stable β alloys found in single phase β region have no commercial and practical use, the expression β alloys is commonly used only for metastable β alloys (see Fig. 2.4). A metastable β alloy can be defined as any titanium alloy with enough β stabilizer content to retain the β phase upon cooling from β phase field to room temperature. In other words, no martensitic decomposition takes place during quenching [4]. The principal advantages of these alloys are good response to heat treatment, ductility, weldability and high strength. Examples of β titanium alloys include Beta C, Beta CEZ, Ti-15-3, Beta 21S or LCB which was the subject of this study. As mentioned in Section 2.2.1, β alloys can be classified into β isomorphous and β eutectoid systems according to the type of alloying additions. The observations indicate that the more the alloying element lies to the right of the transition metal period of the periodic table, the more the system changes from β isomorphous to β eutectoid [2]. Other way of classifying β titanium alloys is based on solute content, in particular (a) solute lean and (b) solute rich [23]. According to this, alloys which form ω during low temperature ageing would be defined as solute lean, whereas alloys which are too stable to decompose isothermally to a $\beta + \omega$ mixture would be classified as solute rich (see Fig. 2.4).

2.4 Phase transformations

A variety of phase transformations can take place in titanium alloys during different thermo-mechanical treatments. Combinations of some of them are commonly used to improve mechanical properties of the material. Here we will focus only on phase transformations relevant for this study, i.e. important phase transformations in metastable β titanium alloys. In particular, we will concentrate on $\beta \rightarrow \omega$, $\omega \rightarrow \alpha$ and $\beta \rightarrow \alpha$ transformations.

2.4.1 $\beta \rightarrow \omega$

The first of the above mentioned transformations, $\beta \rightarrow \omega$, is a displacive shuffle transformation. It is well known that ω phase grows in certain orientations with

respect to β matrix. Their orientation relationship can be described as [24]

$$(0001)_\omega \parallel (111)_\beta \quad (2.4)$$

$$[11\bar{2}0]_\omega \parallel [011]_\beta \quad (2.5)$$

Since there are four sets of $(111)_\beta$ planes, there are four possible crystallographic orientations of ω cells in the parent β grain.

Several models were proposed to explain the mechanism of ω formation. The most successful one was developed by de Fontaine [11]. This model viewed the β bcc lattice as a set of $(111)_\beta$ planes perpendicular to the $[111]_\beta$ direction. The lattice was then subjected to a sinusoidal displacement wave of longitudinal mode with wave vector $k = \frac{2}{3}[111]_\beta$ and propagating in the $[111]_\beta$ direction. The displacement wave and the corresponding collapse of neighbouring planes is illustrated in Fig. 2.5 [25]. According to this figure, the $(111)_\beta$ planes labeled by

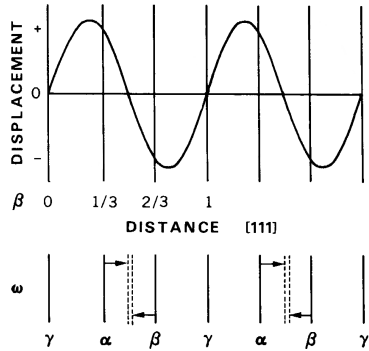


Figure 2.5: Effect of the displacive wave ($k = \frac{2}{3}[111]_\beta$) on the bcc lattice of the β phase, producing ω structure [25]

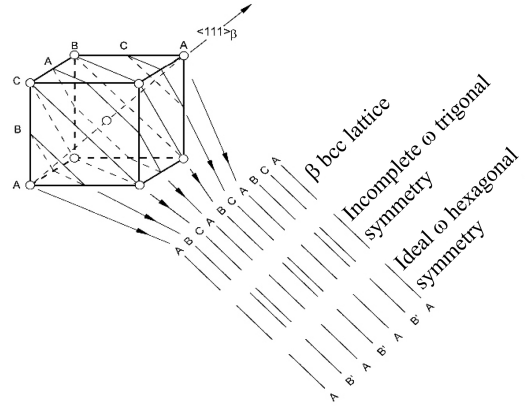


Figure 2.6: The $\beta \rightarrow \omega$ transformation represented as a displacement wave mechanism. The incomplete (trigonal symmetry) and complete transformation (hexagonal) is shown [6]

integers $0, 1, \dots$ do not move, while the planes labeled $1/3, 2/3$ move towards the intermediate $1/2$ position. As a result of this displacement, the stacking sequence of the bcc $(111)_\beta$ planes changes from $ABCABC \dots$ to $AB'AB' \dots$, where A planes remain unchanged and B' planes correspond to the collapsed neighbouring bcc planes (see Fig. 2.6 [6]). The beauty of this model lies in the fact that it relates the major instability that may arise in the bcc lattice to be the one leading to the $\beta \rightarrow \omega$ transformation [26].

The formation of ω phase has a significant impact on mechanical properties of β titanium alloys. The precipitation of the metastable ω particles results in an increase of yield strength and a reduction of ductility of the alloy.

2.4.2 $\beta \rightarrow \alpha$

Let us now focus on formation of α phase in the β matrix. The nucleation and growth of α particles from the high temperature β phase has been an important issue for many researches due to its effect on mechanical properties of titanium

alloys. As it was stated before, the precipitation of α phase has a great impact on toughness, ductility and tensile and fatigue properties of $\alpha + \beta$ and β alloys.

The growth of α phase in β matrix is a diffusional transformation and as such is controlled by two processes: migration of the α/β interface and diffusion of solute atoms across the interface. During growth of the precipitates, both processes occur simultaneously and the slower one determines the growth rate. When the diffusion of solute atoms is slower than the interface migration rate, the interface will move as fast as the diffusion allows and the transformation is said to be diffusion controlled. On the other hand, when the interface mobility is the limiting process, interface controlled transformation occurs.

For α phase precipitated in the β matrix, the following Burgers orientation relationship is observed between the hcp and bcc structures:

$$(0002)_\alpha \parallel (110)_\beta \quad (2.6)$$

$$[11\bar{2}0]_\alpha \parallel [\bar{1}\bar{1}1] \quad (2.7)$$

There are four known heterogeneous nucleation sites for α precipitation in β alloys: β/β grain boundaries, previously formed α particles, ω particles and dislocations. Moreover, it has also been argued that solute lean β phase formed by phase separation in β titanium alloys does contribute to α phase nucleation [21]. In $\alpha + \beta$ alloys martensite plates provide one more nucleation site.

The morphology and distribution of α phase depends on its precursor. According to various authors, three types of α particles are formed in β alloys based on ageing temperature and the corresponding nucleation sites [27, 28]:

1. At relatively low ageing temperatures (< 450 °C), extremely fine α particles are observed uniformly dispersed throughout the β matrix. Due to α particle size and distribution bearing a close resemblance to that of preceding $\beta + \omega$ structure, it has been widely assumed that ω phase is a precursor for α phase formation. The different mechanisms how ω acts as a nucleation site for α are discussed in Section 2.4.3.
2. Above 450 °C there is sufficient thermal activation to allow nonuniform nucleation of α phase, which exhibits no relationship to previous dispersion of ω particles in the β matrix. The particles of α phase formed during this temperature regime have high aspect (length to width) ratio and the resulting microstructure is often described as patchy.
3. A third precipitation regime is observed at high ageing temperatures (> 650 °C). In this regime, α phase forms as a more or less continuous layer along β/β grain boundaries. This type of α morphology is often seen along with a small number of randomly dispersed intragranular α precipitates.

2.4.3 $\omega \rightarrow \alpha$

Mechanisms of ω assisted nucleation of α phase are well known from the literature. The nuclei of the α phase form in the following ways:

1. At interface dislocations or ledges which develop on the ω/β interfaces. This nucleation is typical for high misfit systems which exhibit cuboidal shaped ω particles [21]. A detailed study of α nucleation at ω/β interfaces was done by Williams and Blackburn [19]. They showed that when the critical misfit is exceeded, interfacial edge dislocations form in $\langle 110 \rangle_\beta$ directions. The formation of dislocation is then followed by nucleation of α “rod” lying in the same orientation as the corresponding dislocation. Such α phase was assumed to nucleate at the dislocation or adjacent to it due to stress fields induced by the dislocation. α phase nucleated at ω/β interface was found to have following orientation relationship with β and ω phases:

$$(0001)_\omega \parallel (\bar{1}2\bar{1}0)_\alpha \parallel (\bar{1}11)_\beta \quad (2.8)$$

$$(\bar{1}\bar{1}20)_\omega \parallel (0001)_\alpha \parallel (0\bar{1}1)_\beta \quad (2.9)$$

$$[1\bar{1}00]_\omega \parallel [10\bar{1}0]_\alpha \parallel [211]_\beta \quad (2.10)$$

Finally, the α rods grow and eventually consume the ω particles.

2. Directly from the ω particles by a monotropic reaction both in low and high misfit systems [21]. This regime was observed during ageing at temperatures near the stability limit of ω phase, i.e. where the ω phase is stable for relatively short times. It has been shown recently by the means of high-resolution electron microscopy (HREM) that the α plates form in the core of ω particles mainly by a displacive transformation [29]. A strict orientation relationship was observed between α and ω phases. The nucleated α phase then grows by a diffusive mechanism at the expense of ω particles.
3. At some distance from the ω/β interface due to local α stabilizer Al enrichment in this region. This enrichment could arise from the interaction of the stress field associated with the ω/β interface and the diffusion of solute elements [30].

2.5 Previous works done on phase transformations in LCB

Probably the most related work to this study is the master’s thesis by B. Kokuoz [31]. The present work is basically a continuation of the research begun by the aforementioned author. The main objective of her work was to bring an understanding to the precipitation and growth kinetics of various α morphologies forming during high temperature annealing of TIMETAL LCB. In particular, the author investigated the following aspects of phase transformations:

1. The effect of solution treatment conditions on the β/β grain boundaries and their structure.
2. The heterogeneous grain boundary nucleation and growth of various morphologies of α phase during high temperature ageing at temperatures close to the β -transus.
3. The role of crystallographic orientation between these α morphologies and the β phase in overall transformation kinetics.

To eliminate any prior intragranular nucleation sites for α phase, the material was first solution treated at 820 °C for 30 min. This solution treatment was immediately followed by heat treatments at 700 °C, 715 °C, 730 °C and 750 °C terminated by water quenching after various selected ageing times. These temperatures were chosen to avoid the nose of the TTT (Time–Temperature–Transformation) diagram for TIMETAL LCB, thereby preventing intragranular precipitation of α phase at early stages of the transformation. The sequence of morphological evolution of precipitated α phase was examined by the means of scanning electron microscopy (SEM), electron back-scatter diffraction (EBSD) and quantitative image analysis. The results indicated that after an incubation period of 1 – 3 min, the α phase nucleation starts first on triple junctions followed by nucleation at high-angle grain boundaries. Quantitative image analysis measurements showed that the amount of transformed grain boundary area increased with increasing ageing time at a given ageing temperature. Moreover, the grain boundary α distribution was found to be more homogeneous with increasing ageing temperature. After longer ageing times, decomposition of β phase to plate-like α precipitates was observed. These α precipitates, referred to as Widmanstätten side plates, were shown to grow directly from grain boundary α by high magnification SEM microscopy. With continued ageing, intragranular α plates were found to precipitate near the Widmanstätten side plates.

For the purpose of the present work, two conditions after high temperature ageing treatment with the same volume fraction of grain boundary α were selected (see Table 3.3 in Section 3.2.1). In the following study, the influence of subsequent low temperature ageing on phase transformations and the corresponding ageing response was examined.

The work done by Azinzadeh and Rack [30] deals with the dependence of ageing response of TIMETAL LCB on the reaction path and ageing temperature and time. After solution treatment, the studied material was either artificially aged at temperatures between 300 °C and 750 °C for times up to 1024 h or re-solution treated and isothermally aged by direct quenching to selected ageing temperatures. During artificial ageing, the growth of ellipsoidal ω particles (formed during quenching from the solution treatment temperature) was observed below 350 °C up to ageing times of 1024 h. In the temperature range of 390 – 460 °C the precipitation of α particles associated with ω phase by Burgers relationship occurred. Artificial ageing at temperatures between 520 °C and 650 °C resulted in formation of needle-shaped intragranular α and an almost continuous α grain boundary film. No ω phase was observed in this temperature range and above. At the highest ageing temperatures, 700 – 750 °C, the heterogeneous grain boundary α formation became the dominant reaction. Isothermal ageing showed evidence of spontaneous formation and growth of ω phase at low ageing temperatures (about 350 °C). No α phase precipitation was observed up to 390 °C. At higher ageing temperatures (460 °C and above) both homogeneous and heterogeneous nucleation of α phase occurred. It was shown that in this temperature range, lower ageing temperatures promote homogeneous nucleation, while higher temperatures favor heterogeneous nucleation processes.

Another report on ageing behaviour of TIMETAL LCB was given by Sakamoto et al. [32]. The effect of microstructure evolution on hardness of the material was investigated in this study using transmission electron microscopy (TEM),

high resolution electron microscopy (HREM), X-ray diffraction (XRD) and microhardness measurements. The material was solution treated and subsequently aged at four different temperatures in the range of 350 – 600 °C for ageing times between 5 min and 10h. ω phase was observed in all samples aged at 350 °C and 400 °C and in the sample aged 500 °C for 5 min. It was shown that material in which ω assisted nucleation of α phase occurred, exhibited significantly higher hardness.

3. Experimental procedures

3.1 Studied alloy

For the purpose of this study titanium alloy called TIMETAL LCB was used. This alloy is a metastable β alloy developed by TIMET to address the need for a less expensive titanium alloy (LCB is an abbreviation of Low Cost Beta) with mechanical properties comparable to other β titanium alloys. The price reduction was achieved by using Fe/Mo β stabilizing addition rather than expensive alloying elements such as V or Nb. This lowered the production cost to roughly the same level as that of CP (commercially pure) titanium. Depending on the particular alloy, this can represent a reduction of more than 50% in production cost alone [7].

LCB was designed primarily for use in non-aerospace applications such as suspension springs and torsion bars in automobiles or as high-strength, corrosion resistant components where so far employed alloys had insufficient strength or were too costly [5].

The typical room temperature properties of TIMETAL LCB along with its ultimate tensile strength (UTS) and elongation for solution treated condition are given in Table 3.1 [33]. The tensile properties are strongly dependent on ageing conditions – whereas tensile strength is improved by ageing treatment, elongation tends to change inversely with strength.

Density	4.8 g/m ³
Specific heat	519 J/(kg·K)
Elastic modulus	110 – 117 GPa
UTS	1035 MPa
Elongation	16 %

Table 3.1: Typical properties of TIMETAL LCB

According to Equation 2.3, the molybdenum equivalency of TIMETAL LCB is 18.4, which classifies it as a solute lean β titanium alloy. A comparison to other well-known β titanium alloys is shown in Figure 3.1 [7]. The melting point of TIMETAL LCB lies in the range of 1650 ± 15 °C and the β -transus is 790 °C [31]. The chemical composition is shown in Table 3.2.

Element	Ti	Mo	Fe	Al
Wt. %	87.2	6.8	4.5	1.5
At. %	89.8	3.5	4.0	2.7

Table 3.2: Chemical composition of TIMETAL LCB

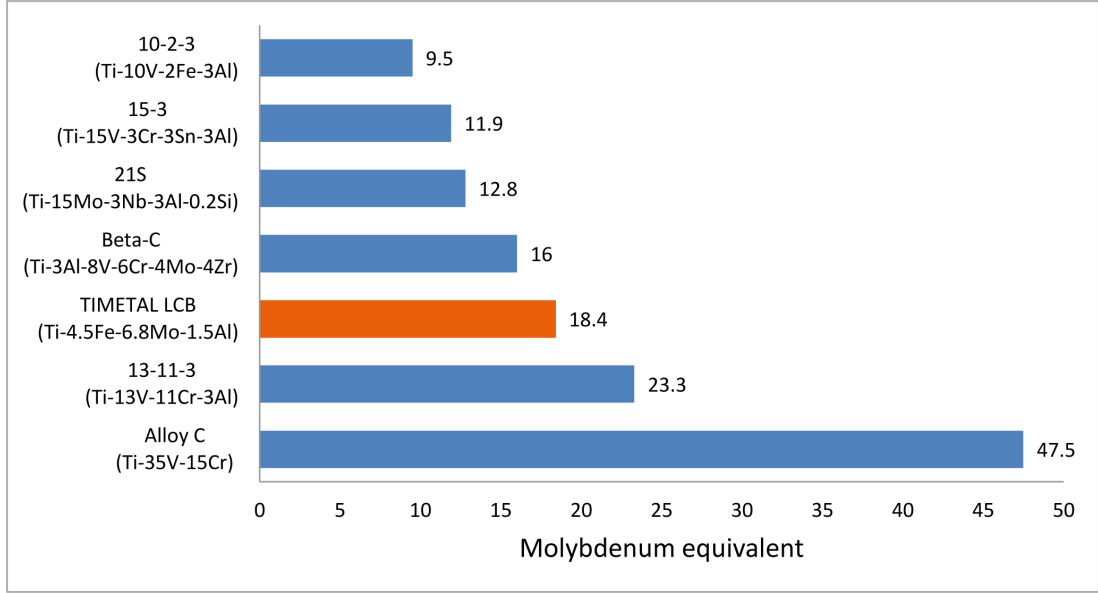


Figure 3.1: The molybdenum equivalent of various β titanium alloys

3.2 Heat treatment

3.2.1 High temperature annealing

Two initial conditions of the material (15 mm diameter bars) were prepared by solution treating in the single phase β region at 820 °C for 30 min. Since this temperature is above the β -transus of LCB, single phase β microstructure was formed. After this treatment, the bars were directly quenched to two different temperatures in the $\alpha + \beta$ phase field in order to precipitate α phase on β/β grain boundaries. The two $\alpha + \beta$ solution treatments are given along with resulting grain boundary α characteristics in Table 3.3. As follows from this table, both

Condition	α/β treatment	Vol.(%)	Thickness (μm)	Contiguity
#1	700 °C, 10 min	1.5	0.26	0.524
#2	730 °C, 50 min	1.5	0.41	0.360

Table 3.3: Grain Boundary Alpha Characterization

$\alpha + \beta$ solution treatments resulted in a fixed grain boundary α volume fraction of 1.5 for both conditions. The conditions 1 and 2 differ in the average thickness and contiguity of grain boundary α . Contiguity is basically a number which determines how continuous the grain boundary α film is. The higher the number, the more continuous the grain boundary α is.

3.2.2 Low temperature annealing

The solution treated rods were cut into individual samples (for detailed description see Section 3.3). To analyze the heating response of the material, the resulting samples were aged in neutral salt baths at 400 °C, 450 °C and 500 °C for ten different times (0.5 h, 1 h, 2 h, 4 h, 8 h, 16 h, 32 h, 64 h, 128 h, 256 h). The

salt baths were used to ensure a defined and identical heating rate for all samples (more than 100 °C/min) and to prevent their oxidation. Increased oxygen content, in fact, significantly influences mechanical properties of the alloy and its phase transformation kinetics. The low temperature treatments were terminated by water quenching to room temperature.

3.3 Sample preparation

The material was cut into 5 mm thick slices utilizing an automatic precision saw Struers Accutom-50 with Struers diamond wafering blade. The blade speed was 1500 rpm and the feed rate 0.005 mm/s. Material cooling during cutting and cutting debris removal was ensured by recirculating water.

For the purpose of microhardness measurements and scanning electron microscopy (SEM), the aged samples were first mounted and then ground and polished using standard metallographic procedures. As scanning electron microscopy requires conductive samples, the chosen mounting material was electrically conductive (PolyFast supplied by Struers). To eliminate any deformation or contamination of the surface layer, approximately 1 mm was removed by grinding on 220 grit (European FEPA grading) SiC grinding paper. Then the samples were ground and polished utilizing 500, 800, 1200, 2400 and 4000 grit SiC papers. Final polishing was done using a vibratory polisher and employing 0.3 μm and 0.05 μm aqueous alumina (Al_2O_3) suspensions and 0.05 μm colloidal silica.

For the X-ray diffraction measurements, the mount was removed and the samples were repolished to remove any oxidized layer which may have formed during storing the samples before X-ray spectroscopy.

For differential scanning microscopy (DSC), small cubes were cut out of the unaged material. The sides of each cube were ground on 600 grit SiC polishing paper to remove surface contamination and deformation induced during cutting. The aim was to produce samples of similar weight, thus all the sample masses were in the range of 140–150 mg. To prevent oxidation during heating in the DSC furnace, a layer of yttrium oxide (Y_2O_3) was sprayed on the resulting samples.

For resistivity measurements, approximately 1 mm thick plates were cut longitudinally from the α/β annealed rod. The final shape in the form of letter “N” was subsequently cut using Struers Accutom-50 precision saw equipped with a diamond wafering blade. Each sample was ground on SiC grinding papers and etched in a Kroll’s reagent (50 ml of distilled water, 4 ml of HNO_3 and 2.5 ml of HF) to remove any surface deformation or contamination. Four contacts made from commercially pure titanium wire were placed on the sample. The titanium wire was used to minimize the contact resistance between the sample and the probe.

Specimens for tensile tests were machined according to drawing in Figure 3.2 from α/β annealed rods by Beznoska Inc. The samples had circular cross-section with the diameter of 3 mm and the gauge length of 18 mm. The rod was cooled during machining to prevent heating of the material and consequent phase transformations. The surface of each sample was polished to prevent surface crack initiation during tensile test which would lead to earlier failure of the specimen.

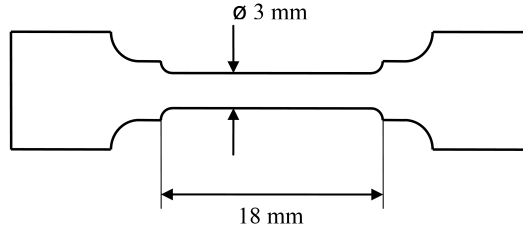


Figure 3.2: The tensile test specimen

3.4 Scanning electron microscopy (SEM)

Direct observations of the microstructure of the material were performed by scanning electron microscope FEI Quanta 200F equipped with a field emission gun (FEG). The accelerating voltage was 10 keV.

The electrons emitted from the field emission gun (cathode) are first accelerated by the potential difference between the cathode and anode. The electron beam then passes through a series of magnetic lenses designed to focus the beam. Finally, the beam is deflected in the x and y axes by a pair of scanning coils, thus scanning in a raster fashion over a rectangular area of the sample surface.

As the primary beam hits the sample, the electrons interact with the atoms of the material within a volume known as the interaction volume. The size of the interaction volume depends on the energy of the primary beam, the sample density and the atomic number of the atoms in the specimen. The interaction between the electron beam and the sample results in the formation of different signals which contain information about the sample, e.g. its topology or composition.

One of the most important signals are *back-scattered electrons* (BSE). This type of signal consists of high-energy electrons originating from the primary beam, which were reflected (back-scattered) by elastic interactions with the atoms in the sample. The amount of back-scattered electrons depends on the atomic number of the specimen. Heavy elements with higher atomic number scatter the electrons more strongly than light elements, therefore the number of back-scattered electrons is higher and the regions with heavier elements appear brighter in the BSE image. For that reason, back-scattered electrons are used to observe the chemical contrast of the specimen. Back-scattered electrons can also be used in electron back-scatter diffraction (EBSD) imaging to determine various crystallographic parameters of the specimen, e.g. the orientation of individual grains, misorientation, grain boundary character distributions etc.

Another common imaging mode employs the signal of *secondary electrons* (SE). These electrons are ejected from the electron shells of specimen atoms by inelastic scattering of the primary beam. They have low energy (< 50 keV), therefore only those secondary electrons which are emitted near the surface can exit the sample and be detected. The amount of secondary electrons emitted from the sample depends on the topology of the surface. More secondary electrons tend to be emitted from steep surfaces and ledges, which results in a three dimensional appearance of the SE image.

An electron from the primary beam can also interact with inner shell electron of specimen atom, ejecting it from its orbital. The atom is left in an excited state

with a missing inner shell electron. An electron from an outer, higher energy shell then fills the inner shell vacancy. The energy difference between the two shells is a characteristic value for each element. This excess energy can be released in two ways. In the Auger process, the energy is used to eject another outer shell electron. In the characteristic X-ray process, the difference in energy is released in the form of an X-ray. The quantity of characteristic X-rays and their energies are measured by an analytical technique called *energy dispersive X-ray spectroscopy* (EDS). As the energies of the X-rays are characteristic for the particular element, the elemental composition of the specimen can be determined [34].

The electron microscope requires a conductive sample which does not charge during the measurement. The charging of the sample is caused by a buildup of excess electrons on the sample surface. This buildup creates an electric field which deflects the primary electron beam. In addition, this undesirable charge may be randomly released from the sample, which creates image artifacts. Therefore, all the samples used for this study were mounted in a conductive mounting material.

3.5 Microhardness measurements

The microhardness measurements were done using Vickers indentation hardness tester Leco M-400-A. In Vickers hardness test, a diamond indenter in the form of a square-based pyramid is used. The angle between the opposite faces of the pyramid is 136° , see Fig. 3.3. The sample is first fastened onto a cross stage

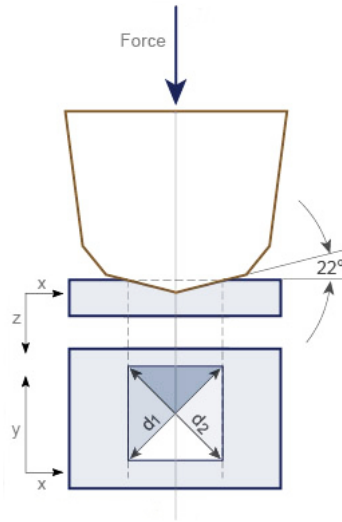


Figure 3.3: Vickers microhardness scheme [35]

and focused. The indenter is then pressed into the surface of the sample with a specified force for a duration of 10 s. After unloading, the hardness value is obtained from the indentation area A as follows [35]:

$$A = \frac{d^2}{2 \sin(136^\circ/2)}, \quad (3.1)$$

where d denotes the average length of the diagonal of the indentation left by the indenter in millimeters. The equation above can be approximated by evaluating

the sine term to give

$$A \approx \frac{d^2}{1,854} . \quad (3.2)$$

The resulting microhardness (HV number) is then determined by the ratio F/A where F is the applied load.

$$\text{HV} = \frac{F}{A} \approx \frac{1,854 F}{d^2} . \quad (3.3)$$

The force applied during the measurements corresponded to the weight of 500 g.

The calculation of the microhardness value from the size of the indentation was done automatically by a computer program Lucia Hardness.

3.6 X-ray diffraction

The measurement of X-ray diffraction (XRD) was done using a powder diffractometer Bruker D8 Advance with focusing Bragg-Brentano geometry ($\theta-2\theta$, with fixed tube and rotating sample), see Fig. 3.4. The diffractometer was equipped with a rotational sample holder and a laboratory Cu tube operated at 40 keV and 40 mA producing CuK_α radiation. The axial divergence of the incident beam was controlled by Soller slits. The diffracted beam was detected by Sol-X energy dispersive point detector.

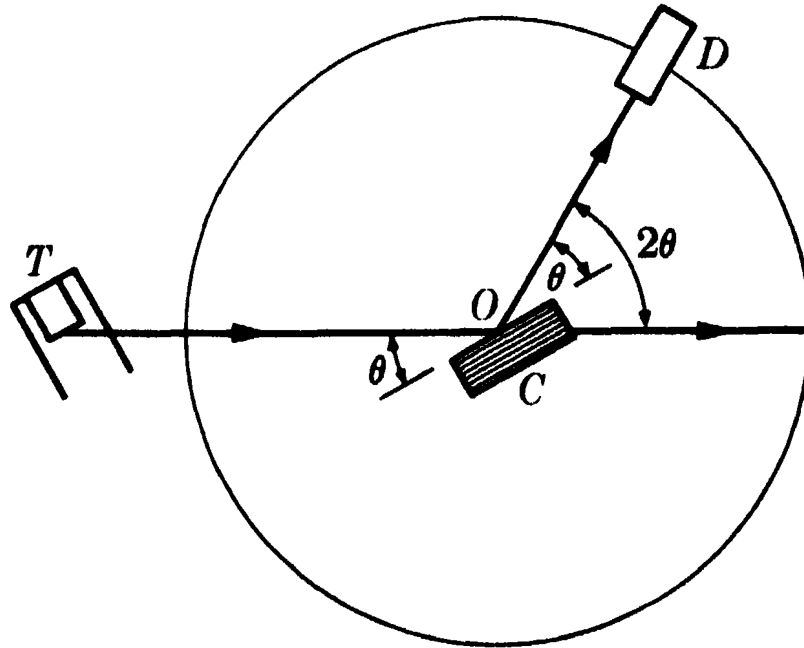


Figure 3.4: Scheme of $\theta - 2\theta$ Bragg-Brentano focusing geometry, X-rays from tube T are incident on a crystalline sample C which rotates about the center of the spectrometer O , D is the detector. The tube is fixed, the sample angle varies as θ and the detector angle varies as 2θ [36]

The principle of X-ray diffraction can be interpreted according to W. L. Bragg as a reflection of incident X-ray beam from periodically spaced lattice planes in the sample. The conditions for a sharp peak in the scattered intensity are: the angle of reflection equals the incidence angle and the reflected rays from successive planes interfere constructively. The incident and reflected rays are shown in Fig 3.5. From this figure it follows that the path difference between the two depicted

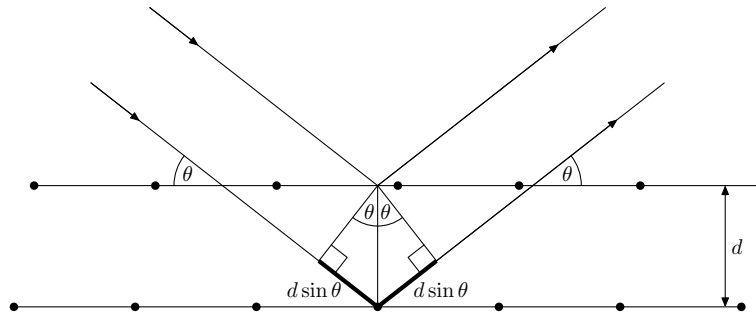


Figure 3.5: A Bragg reflection from a family of lattice planes with lattice spacing equal to d

rays is $2d \sin \theta$, where θ is the angle of incidence and d the interplanar distance. The interference of the X-rays is constructive when the path difference is an integer multiple of the wavelength. This leads to Bragg's law which describes the condition for constructive interference from successive crystallographic planes:

$$n\lambda = 2d \sin \theta, \quad (3.4)$$

where n is an integer known as the order of the corresponding reflection and λ denotes the wavelength [37].

The result of X-ray diffraction measurement is a diffraction pattern – a plot of reflected intensities versus the detector angle 2θ . Strong peaks in the pattern are obtained when scattered waves satisfy the Bragg's law. This intensity profile can be characterized by several parameters: the positions of the diffracted peaks, their width, integral intensity and shape. The peak positions (their 2θ value) provide information about the geometry of the crystal lattice and its lattice parameters. Peak positions are further influenced by residual stresses in the material. The integral intensity of a peak corresponds to the volume fraction of the particular phase. From the peak width the size of coherently scattering domains can be determined. The peak width is also affected by the measuring system. This effect is referred to as instrumental broadening. The instrumental broadening needs to be eliminated during line profile analysis to obtain broadening exclusively due to microstructural effects. Finally, the shape of the peak correlates with the type and distribution of crystallographic defects.

3.7 Differential scanning calorimetry (DSC)

Differential scanning calorimetry (DSC) is a thermoanalytical technique measuring the temperature difference between a sample and a reference which are heated

at the same time. The temperature difference is then plotted as a function of temperature or time and indicates qualitatively the heat exchange. The sample and the reference are both placed in identical environments – ceramic crucibles on separate bases, each of which is equipped with a thermocouple. The sample and the reference (which is usually only an empty crucible) are subjected to a controlled temperature program, in most cases a constant heating rate. Thermal processes in the sample which are associated with phase transformations require more or less heat than the inert reference, which results in the temperature of the sample being lower or higher, respectively. The resulting temperature difference between the sample and reference is then recorded as a peak. The type of the transformation (endothermic or exothermic) determines whether heat is absorbed or released. The presence of an endothermic peak indicates the occurrence of a heat absorbing event, such as melting or dissolution. On the other hand, an exothermic peak occurs as a result of a heat releasing event, such as solidification or precipitation. The orientations of peaks in the DSC measurements done for this study are according to a convention in which exothermic peaks are directed upwards and endothermic downwards [38, 39].

3.8 Resistivity measurement

Studies of the dependence of electrical resistivity on composition and temperature provide information about strengthening mechanisms, phase stability and the electronic structure of alloys. Electrical resistivity measurements may also be employed to detect phase transformations during heating and quenching of the material [17].

The total resistivity ρ of a dilute alloy at a given temperature T can be written as a sum of two components:

$$\rho(T) = \rho_i(T) + \rho_0 , \quad (3.5)$$

where ρ_i is the temperature dependent “ideal” resistivity of the pure host material (phonon scattering) and ρ_0 represents the temperature independent impurity scattering from the solute atoms. This is known as Matthiessen’s rule and will be only valid if the phonon and impurity scattering are independent and the relaxation time is isotropic [40]. The Matthiessen’s rule can also be used to characterize the total resistivity of concentrated and more complex alloys. In this extrapolation, the temperature independent component ρ_0 includes all contributions from scattering due to various disorders in the lattice periodicity (dislocations, particles of different phases, grain boundaries, stress fields, etc.).

The resistivity of the sample was measured by a four probe method to eliminate the resistance introduced by the probes. In this method, two separate pairs of contacts are used. Electrical current is passed through the two outer probes, while the voltage is measured between the two inner contacts. Thus, the voltage drop in the current carrying wires is not measured by the voltmeter. Since the resistance of the voltmeter is very high, the current that flows through it and the connecting leads is almost negligible. Therefore, the voltage drop across the inner contacts is very small. The sample resistance is then calculated as the voltage measured by the inner probes divided by the current flowing through the outer contacts.

3.9 Tensile testing

A tensile test is a fundamental type of mechanical test in which a sample is subjected to uniaxial loading until failure. The specimen is fixed at one end in a static grip, while the other end is pulled at a constant velocity. The typical strain rate ranges from 10^{-4} s^{-1} to 10^{-1} s^{-1} . The applied load is continuously monitored throughout the experiment. The elongation of the sample is most commonly measured by an extensometer. For the purpose of this study, a video extensometer was used. The video extensometer is a device which captures images of the measured sample marked with two dots. The distance between these two markers is then measured in real time while the specimen under test is strained.

During tensile testing, the response of the material to applied force in tension can be determined. Multiple properties such as ultimate tensile strength, yield stress, Young's modulus, strain, ductility or work-hardening characteristics can be found.

The output of a tensile test is a dependence of stress on strain, in a graphical interpretation called the stress–strain curve. In engineering notation, the stress σ is calculated from the applied load F and the initial cross-sectional area of the sample S_0 as follows:

$$\sigma = \frac{F}{S_0} . \quad (3.6)$$

The engineering strain ε is derived from measuring the elongation of the sample and can be obtained by equation:

$$\varepsilon = \frac{\Delta L}{L_0} = \frac{L - L_0}{L_0} , \quad (3.7)$$

where L_0 denotes the original length of the sample, ΔL is the change in its length and L the current length.

A typical stress–strain curve can be divided into two regions – elastic and plastic. The elastic region is observed at the beginning of a tensile test, where stress is linearly proportional to strain. Elastic deformation is caused by stretching of atomic bonds and as such is reversible. In the elastic linear range, the stress–strain curve obeys the Hooke's law:

$$\sigma = E\varepsilon , \quad (3.8)$$

where E is a material constant (Young's modulus) and corresponds to the slope of the stress–strain curve. The Young's modulus can be interpreted as a measure of stiffness of an elastic material. The elastic region ends when the material reaches the yield stress. The yield stress is defined as the applied stress at the onset of the plastic deformation. The plastic deformation is irreversible and its onset is evidenced by a deviation of the stress–strain curve from the elastic line. When the yield stress cannot be exactly determined from the shape of the stress–strain curve, its value is generally set at 0.2% of the plastic strain and is denoted as $\sigma_{0.2}$. As deformation continues in the plastic region, the stress increases due to work hardening θ , which is defined as

$$\theta = \frac{d\sigma}{d\varepsilon} . \quad (3.9)$$

Up to the point where $\theta = \sigma$, the cross-sectional area of the sample decreases uniformly. The contraction of the sample perpendicular to the applied load (transverse strain $\varepsilon_{\text{trans}}$) is related to the elongation of the sample (axial strain $\varepsilon_{\text{axial}}$) by Poisson's ratio ν :

$$\nu = -\frac{d\varepsilon_{\text{trans}}}{d\varepsilon_{\text{axial}}}. \quad (3.10)$$

Further loading beyond the point where $\theta = \sigma$ results in necking of the sample. It is a mode of tensile deformation where the strain is localized in a small region of the sample. This results in quick decrease in local cross-sectional area. In engineering stress–strain diagram, necking is evidenced by a decrease of the curve. Eventually, the neck becomes unstable and the sample fractures.

It should be noted that the engineering stress–strain curve does not give a true indication of the deformation characteristics, since it is based entirely on the original dimensions of the sample. However, these dimensions change continuously during the tensile test. When the changes are taken into account in calculation of stress and strain, a true stress–strain curve (also known as a flow curve) is obtained. The true stress is the load divided by the actual cross-sectional area S of the specimen

$$\sigma_{\text{true}} = \frac{F}{S}. \quad (3.11)$$

The true strain is derived from the incremental increase in length dL divided by the current length L :

$$d\varepsilon_{\text{true}} = \frac{dL}{L} \rightarrow \varepsilon_{\text{true}} = \int_{L_0}^L \frac{1}{L} dL = \ln \frac{L}{L_0}. \quad (3.12)$$

Using Equations 3.7 and 3.12, the relation between true $\varepsilon_{\text{true}}$ and engineering strain ε can be derived:

$$\varepsilon_{\text{true}} = \ln(1 + \varepsilon). \quad (3.13)$$

During plastic deformation, the volume of the sample can be considered as constant – increases in length are offset by decreases in cross-sectional area. This assumption allows us to write:

$$dV = 0 \rightarrow SL = S_0L_0 \rightarrow \frac{S}{S_0} = \frac{L_0}{L}. \quad (3.14)$$

Considering this equation and the definitions of the true stress σ_{true} (Equation 3.11), the engineering stress σ (Equation 3.6) and the engineering strain ε (Equation 3.7), we obtain

$$\sigma_{\text{true}} = \sigma(1 + \varepsilon). \quad (3.15)$$

The Equations 3.13 and 3.15 can be used to derive the true stress–strain curve from the engineering curve up to the point where necking starts. After the onset of necking, the strain is nonuniform in the sample length and the equations are not satisfied. However, complete true stress–strain curve can be drawn if the neck area is monitored during the measurement and appropriate models for stress calculation are used [41, 42, 43].

4. Aims and objectives of the work

The ultimate goal of the research in the present work is to clarify the influence of different high temperature treatments (α/β annealing) and subsequent low temperature ageing on fatigue properties of TIMETAL LCB. Whereas the α/β annealing results in distinct grain boundary α morphologies, the ageing at lower temperatures leads to precipitation of secondary α phase in the interior of the β grains. According to the hypothesis, the morphology and continuity of the primary α phase precipitated along grain boundaries should have minor impact on phase transformations in the material and on its hardness and strength. On the other hand, the fatigue properties of the alloy should be considerably influenced by the grain boundary characteristics. However, before the fatigue tests are performed, a thorough understanding of phase transformations occurring in the material and their influence on mechanical properties is needed.

The novelty of this study lies in employing the combination of high temperature ageing as designed in master's thesis by Kokuoz [31] and low temperature ageing during heat treatment of the material.

This present work focuses in particular on:

- The study of the phase transformations occurring during low temperature ageing in two α/β annealed conditions with different grain boundary α contiguity and thickness at a fixed α volume fraction.
- The characterization of microstructure and phase composition evolution during ageing of TIMETAL LCB.
- Defining the relationship between microstructural and mechanical properties, in particular microhardness and tensile response of the material.

5. Results and Discussion

5.1 Microstructure overview of the initial state of the material

The microstructure of the studied alloy TIMETAL LCB consists of equiaxed grains with average sizes of approximately $100\ \mu\text{m}$. The initial state of condition 2 is shown in Fig. 5.1 which was obtained in scanning electron microscope using back-scattered electrons. In this figure, the contrast between individual grains is caused by channelling of the electrons down the lattice planes. The channelling contrast depends on the relative orientation between the incident electron beam and the crystal lattice. Moreover, Fig. 5.1 shows the primary grain boundary α (dark lines) which precipitated on some of the β/β grain boundaries during α/β solution treatment. Two of these grain boundaries where α phase precipitated are indicated by arrows.

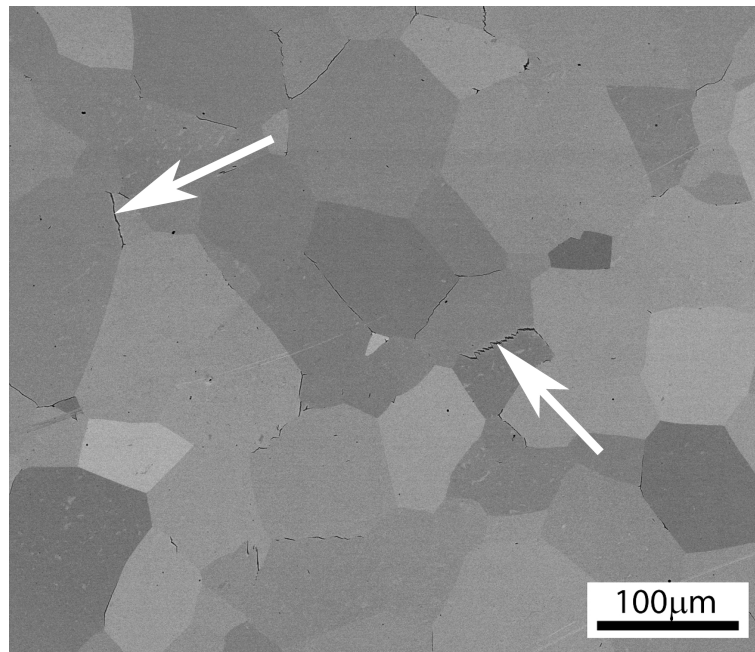


Figure 5.1: The grain structure of an initial state of TIMETAL LCB

The typical microstructure of both initial states of condition 1 and 2 (see Table 3.3) is shown in Fig. 5.2. Dark primary α phase is apparent at grain boundaries of lighter grey β matrix. Note that the grain boundary α film in condition 2 is approximately twice as thick as in condition 1, which confirms the grain boundary α characterization in Table 3.3. In Fig. 5.2, white areas are visible inside the β matrix. These are probably polishing artifacts and have no relevant physical interpretation.

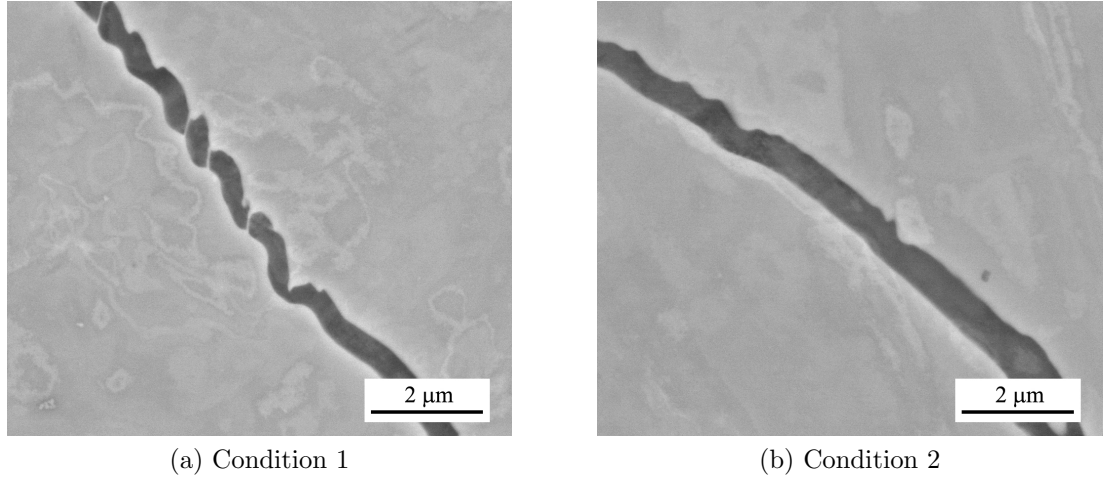


Figure 5.2: The initial state of the material; grain boundary α is shown

5.2 Resistivity measurement

The temperature dependence of resistivity was measured in situ utilizing a home-made programmable furnace. A four probe experimental arrangement was used as described in Section 3.8. The electrical current was supplied by Keithley 2420 DC current source, which also precisely measured the electric current. The voltage across the sample was measured by Keithley 2182 nanovoltmeter.

Figure 5.3 shows a temperature dependence of resistivity (normalized to the initial value ρ_0) during heating of a sample made from condition 1 at the heating rate of 5 °C/min. A comparison with the curve obtained by differential scanning calorimetry at the same heating rate indicated by a grey dashed curve is also shown. The onsets of individual resistivity peaks correspond to the DSC peaks quite accurately. The resistivity curve is divided into six sections according to the phase transformations occurring during heat-up of the material and resulting changes in resistivity evolution. The following discussion of phase transformations resulting in the evolution of resistivity curve are based on previous findings by other authors [44], [45]. Further research has to be done for example by means of transmission electron microscopy in order to prove the following hypotheses.

The negative temperature dependence of resistivity in the first section of Fig. 5.3 is generally attributed to reversible dissolution of athermal ω phase, which was formed during quenching of the alloy [46]. This diffusionless transformation (as indicated by the reversibility) is a displacive process described in Section 2.4.1. During dissolution of ω particles, the β/ω interfaces and related stress fields disappear. This results in decrease in conduction electron scattering and therefore the resistivity drops. Between approximately 210 °C and 370 °C, the increase in resistivity may be attributed to the formation of isothermal ω by a diffusional and thus irreversible process. From 370 °C (region III in Fig. 5.3), another decrease of resistivity is observed. This drop is explained by progressive vanishing of isothermal ω phase through $\omega \rightarrow \alpha$ transformation and $\omega \rightarrow \beta$ dissolution. These two processes lead to the relaxation of stresses in the material, which results in the decrease of the resistivity. In this temperature range the β , ω and α phases coexist. The authors in [44] refer to α phase precipitated in this

temperature range as α nanophase due to small proportions of its particles. The temperature range of approximately 500 °C – 600 °C (denoted by IV in Fig. 5.3) corresponds to the growth of α phase particles, until the equilibrium composition is reached. The subsequent decrease in resistivity in region V in Fig. 5.3 is caused by dissolution of α phase precipitates due to decreasing equilibrium content of α phase. Naturally, lower amounts of α particles correspond to fewer scattering centres for the electrons, which results in lower resistivity. Finally, at approximately 770 °C, a β -transus is observed as evidenced by an increase in resistivity in the temperature range where only β phase is stable (denoted by VI in Fig. 5.3).

The resistivity evolution was also measured during heating at the rate of 50 °C/min (sample from condition 1). The resulting curve is shown in Fig. 5.4 (in black) along with the corresponding measurement performed by differential scanning calorimetry (grey dashed curve).

As it can be seen, the shape of resistivity curve at the heating rate of 50 °C/min is very similar to the one observed at 5 °C/min, the only differences being in the onsets of individual reactions. The first decrease in resistivity (region I in Fig. 5.4) is also caused by reversible dissolution of athermal ω . However, the onset of the next phase transformation, the formation of ω isothermal, is reached at much higher temperature compared to the heating rate of 5 °C/min (approximately 210 °C and 320 °C for 5 °C/min and 50 °C/min, respectively). This effect is due to the diffusional character of the transformation. As a diffusional process, the formation of isothermal ω phase will go as fast as the diffusion rate will allow. This time lag results in a later onset of the transformation in relation to temperature at the faster heating rate. The decrease in resistivity between 420 °C and 520 °C (denoted by III in Fig. 5.4) corresponds to ω dissolution and ω assisted α nucleation, similarly to the lower heating rate. The onset of this process is again slightly shifted towards the higher temperatures during heating at the rate of 50 °C/min, as expected from a diffusional transformation. The region IV in Fig. 5.4 and the corresponding increase in resistivity is caused by the diffusional $\beta \rightarrow \alpha$ process. This reaction is governed by the diffusion of α stabilizing element Al to the growing α phase and the simultaneous rejection of heavier β stabilizers Mo and Fe into the β matrix. This diffusional transformation requires a certain amount of time, therefore, the region IV extends to higher temperatures at the heating rate of 50 °C/min, compared to the lower heating rate 5 °C/min. On the other hand, the region V in Fig. 5.4, which is attributed to the dissolution of α particles back to β phase, spans over a much narrower temperature range. Moreover, the resistivity in this region decreases only very slightly which indicates that due to different phase transformation kinetics during the faster heat-up the α phase dissolution may be overlapped by another process compensating the resistivity decrease. However, exact explanation would require a more thorough research employing for example in situ TEM (transmission electron microscopy) heating. Finally, at approximately 780 °C, β -transus and consequent increase in resistivity is observed.

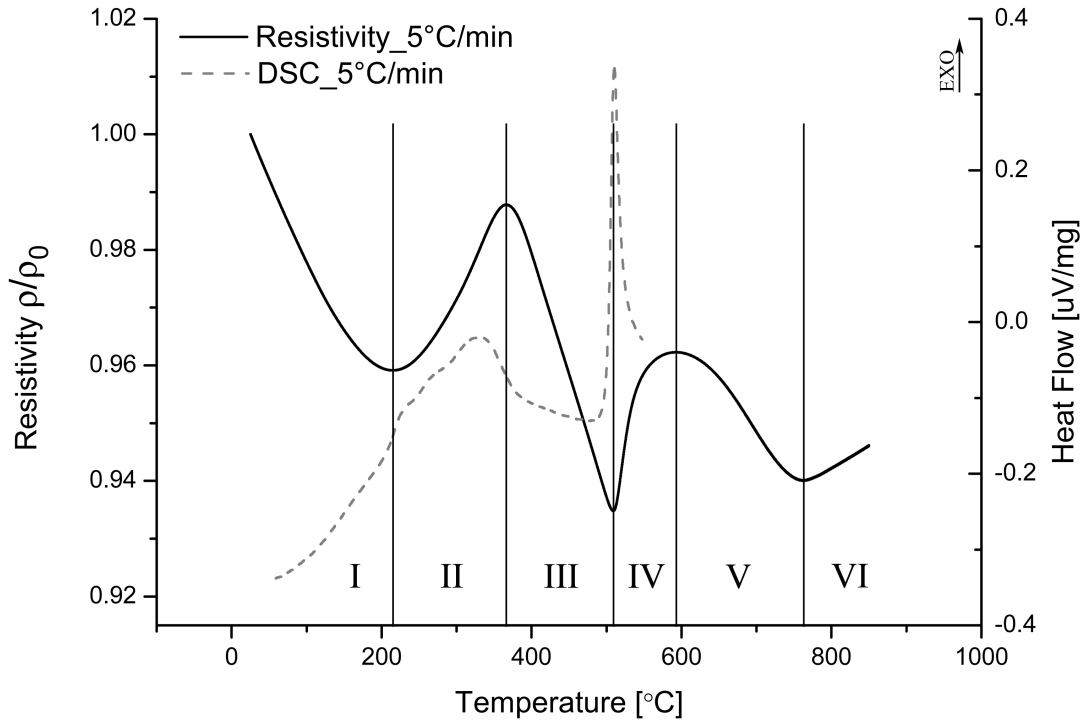


Figure 5.3: The temperature dependence of resistivity at the heating rate of 5 °C/min (black solid curve) and a corresponding DSC measurement at the same heating rate (grey dashed curve)

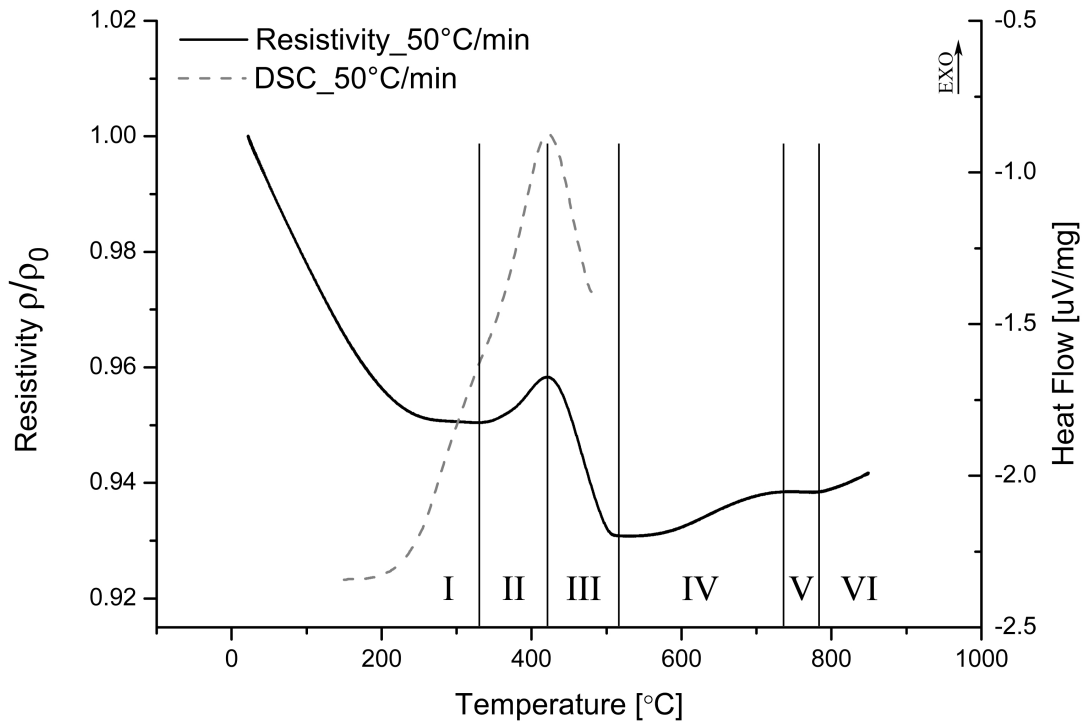


Figure 5.4: The temperature dependence of resistivity at the heating rate of 50 °C/min (black solid curve) and a corresponding DSC measurement at the same heating rate (grey dashed curve)

5.3 Differential scanning calorimetry

The differential scanning calorimetry measurements were performed on Netzsch calorimeter DSC 404 Pegasus. The sample was held in a static argon atmosphere during the whole measurement. Two heating rates were selected for this study – 5 °C/min and 50 °C/min.

Figure 5.3 shows a record of variations of DSC signal with increasing temperature. In this case, the temperature was increased by 5 °C per minute up to 550 °C. This slow scan rate was chosen for the initial observations of phase transformations occurring in the material. At slow heating rates, longer time is available for each phase transformation, therefore, the phase transformations overlap less and the peaks observed in the DSC data are separated. Furthermore, lower heating rate also provides longer reaction times at a given temperature and therefore a greater amount of transformation products forming. On the other hand, at higher heating rates, different phase transformation kinetics may lead to observation of fewer peaks and fewer reactions.

Similarly to the discussion of the resistivity data, the following explanation of processes taking place in the alloy is based on previous studies on titanium alloys [44], [45]. Region I in Fig. 5.3 (approximately up to 210 °C) corresponds according to the resistivity results to reversible diffusionless dissolution of athermal ω phase. However, in this temperature range, no peak in the DSC data is observed. This may be caused by the fact that this displacive transformation described in Section 2.4.1 has very low latent heat, therefore, the differential scanning calorimetry is not able to detect it. Between approximately 210 °C and 370 °C (region II), the isothermal ω particles precipitate irreversibly, implying a diffusional phenomena. At higher temperatures (370 °C – 500 °C, part III in Fig. 5.3), ω assisted heterogeneous nucleation of α phase occurs accompanied by ω phase dissolution. In this temperature range, only a weak signal in DSC data is observed. When the material is heated further (region IV in Fig. 5.3), a sharp peak is observed in the DSC curve. This effect results from the growth of α particles and direct $\beta \rightarrow \alpha$ transformation.

In order to observe the differences between phase transformations occurring in the material at faster heating rates, scanning rate of 50 °C/min was studied. This rate was the highest one the measuring instrument could handle, therefore, it was the closest one to the heating rate achieved in the salt baths during low temperature ageing treatments. The DSC curve obtained at the heating rate of 50 °C/min is shown in Figure 5.4 along with the resistivity evolution at the same heating rate. In this figure, one peak is evident approximately at the temperature of 450 °C.

As Fig. 5.4 indicates, the three temperatures chosen for low temperature ageing treatment used in this work to study the ageing response of α/β annealed material (400 °C, 450 °C and 500 °C) were selected appropriately. The lowest ageing temperature corresponds to the region where isothermal ω forms. The second ageing temperature, 450 °C, lies in the temperature range in which the ω phase dissolves and α particles precipitate. The temperature of 500 °C corresponds to the end of the region III in Fig. 5.4 where ω phase is almost dissolved. Thus, different character of phase transformations can be expected during ageing at 400 °C, 450 °C and 500 °C.

5.4 Microhardness measurement

Microhardness measurement was done on each aged sample of both conditions 1 and 2 as well as on the two initial states. In order to obtain good statistics, ten indentations spaced 0.5 mm apart were made on each sample. The resulting values of microhardness were then calculated automatically for individual indentations according to equation 3.3 by a computer program Lucia Hardness. Mean and standard deviation of microhardness were then computed from the ten indentations. These values are listed in Table 5.1. It should be noted that the real error is greater than the standard deviation obtained from ten indentations on each sample. As the diagonal lengths of the indentations were measured by a manual point-and-click method, the results of microhardness measurements are prone to a certain systematic error caused by the subjectivity of the operator.

The variations in the microhardness with ageing time for each condition and ageing temperature are plotted in Fig 5.5. For clarity, the three different ageing

	condition 1			condition 2		
	400°C	450°C	500°C	400°C	450°C	500°C
0h	343.0 ± 3.6			341.3 ± 3.8		
0.5 h	482.6 ± 5.2	455.9 ± 6.4	455.9 ± 4.7	492.3 ± 8.8	473.2 ± 4.9	449.5 ± 3.9
1 h	490.9 ± 4.7	482.4 ± 5.3	493.3 ± 4.0	497.8 ± 4.8	488.2 ± 3.7	497.4 ± 2.5
2 h	499.2 ± 5.8	536.1 ± 4.4	500.7 ± 5.8	505.8 ± 5.8	535.2 ± 4.7	503.4 ± 4.5
4 h	510.0 ± 3.5	550.7 ± 5.0	491.7 ± 4.6	515.9 ± 2.4	550.0 ± 3.6	495.5 ± 4.2
8 h	525.7 ± 3.7	545.6 ± 6.6	491.7 ± 4.8	525.7 ± 5.3	547.8 ± 5.6	493.0 ± 3.9
16 h	529.9 ± 5.3	544.2 ± 4.0	503.6 ± 4.4	532.6 ± 4.4	551.8 ± 5.9	505.9 ± 2.8
32 h	537.9 ± 4.8	541.0 ± 4.5	490.7 ± 3.1	542.8 ± 2.8	548.1 ± 4.0	496.6 ± 3.7
64 h	548.4 ± 3.9	536.8 ± 5.0	473.3 ± 3.7	553.3 ± 2.6	543.3 ± 4.2	479.8 ± 4.0
128 h	555.2 ± 5.3	533.7 ± 3.9	461.9 ± 3.9	557.5 ± 4.7	536.8 ± 3.2	463.5 ± 4.0
256 h	556.7 ± 4.1	505.9 ± 6.2	449.8 ± 2.8	555.6 ± 2.6	512.4 ± 4.3	451.0 ± 4.3

Table 5.1: Microhardness measurement results

temperatures were separated into three individual graphs. The microhardness evolution for both conditions is compared for ageing at 400 °C in Fig. 5.6, for 450 °C in Fig. 5.7 and for 500 °C in Fig. 5.8. The above mentioned figures show that condition 1 and condition 2 do not differ significantly in the development of microhardness during ageing.

First, the lowest ageing temperature (400 °C, see Fig. 5.6) will be discussed. Initial rapid increase in microhardness was observed in the first 30 min of ageing. The increase corresponds to the growth of particles of the ω phase, which form strong and efficient obstacles for dislocation movement due to their small proportions, homogeneous distribution and relatively high volume fraction. With continued ageing the microhardness steadily increases and reaches its maximum approximately after 128 h of ageing treatment. The increasing microhardness indicates the presence of ω particles and evolution of fine microstructure resulting in age hardening of the material.

At 450 °C, the microhardness reached its maximum much earlier (see Fig. 5.7). The highest hardness values are observed between 4 – 16 h of ageing. With increasing ageing time, the microhardness decreases slightly and finally drops visibly between 128 h and 256 h. The slow decrease suggests the dissolution of ω

phase followed by coarsening of secondary α phase which was formed by $\omega \rightarrow \alpha$ transformation. The rapid decrease of microhardness in samples aged for the longest time (256 h) at 450 °C corresponds to overageing of the alloy. In an overaged sample the secondary α particles are too coarse and thus cease to be effective obstacles for dislocations. Therefore, the hardness of the material drops.

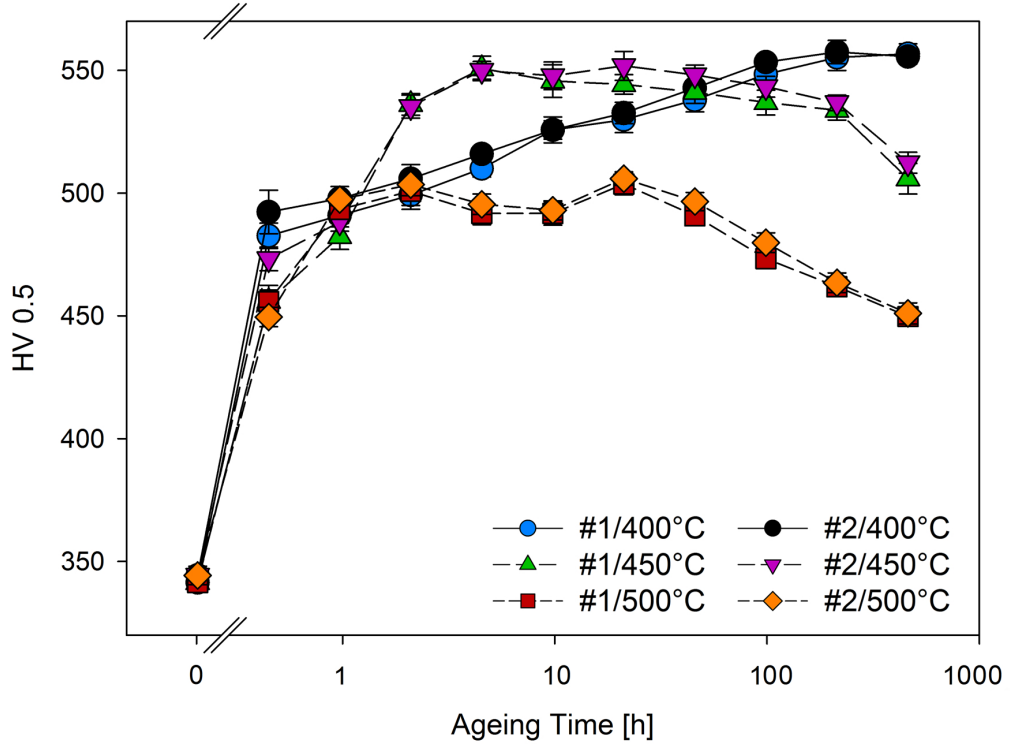


Figure 5.5: Evolution of microhardness with increasing ageing time; condition 1 and 2 aged at 400 °C, 450 °C and 500 °C are shown

At the beginning of ageing at the highest ageing temperature (500 °C), a steep increase in microhardness is observed as well (see Fig. 5.8). The maximum of microhardness is reached already after 2 h. However, the comparison of microhardness variations for all ageing temperatures in Fig. 5.5 indicates that the maximum at the highest temperature is much lower than the respective maxima at lower ageing temperatures 400 °C and 450 °C. Nucleation processes, during which the ω phase dissolved completely and was replaced by secondary α lamellae, resulted in the formation of a second microhardness peak after 16 h of ageing. Finally, overageing and corresponding decrease of hardness with increasing ageing time was observed.

The following conclusions may be drawn from microhardness measurements:

- With increasing ageing temperature, the maximum of microhardness is reached after shorter ageing time. It is evident from Fig. 5.5 that at 400 °C the highest achieved value occurs after 256 h, at 450 °C the peak microhardness is reached after 8 h and at 500 °C after 2 h only.
- The highest value of microhardness is significantly lower after ageing at

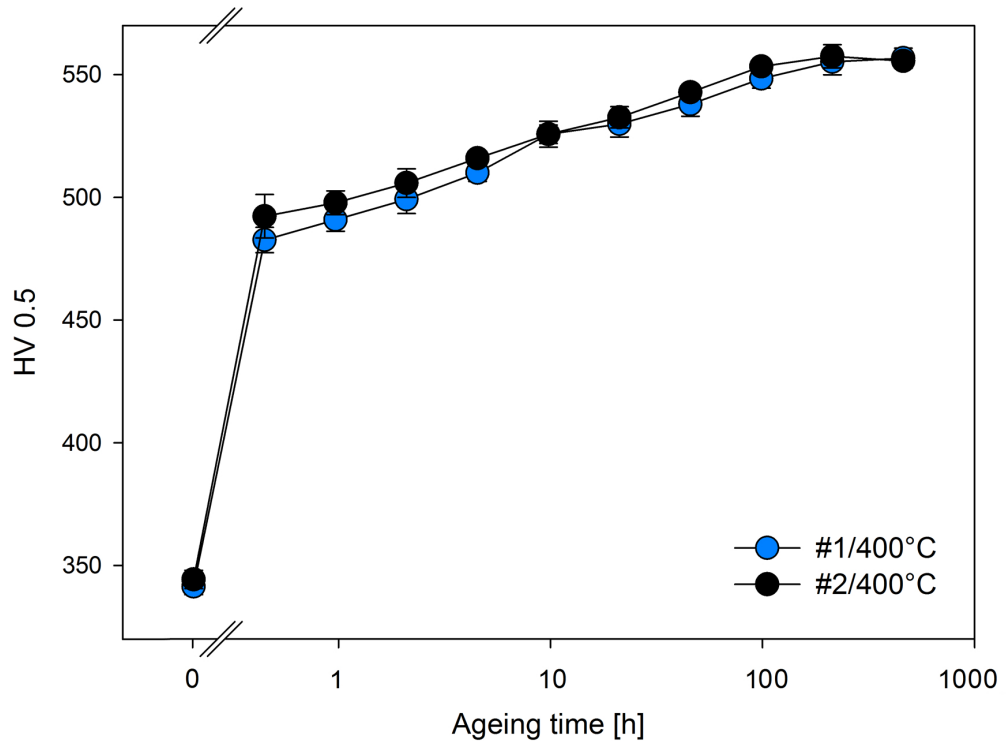


Figure 5.6: Microhardness evolution for condition 1 and 2 aged at 400 °C

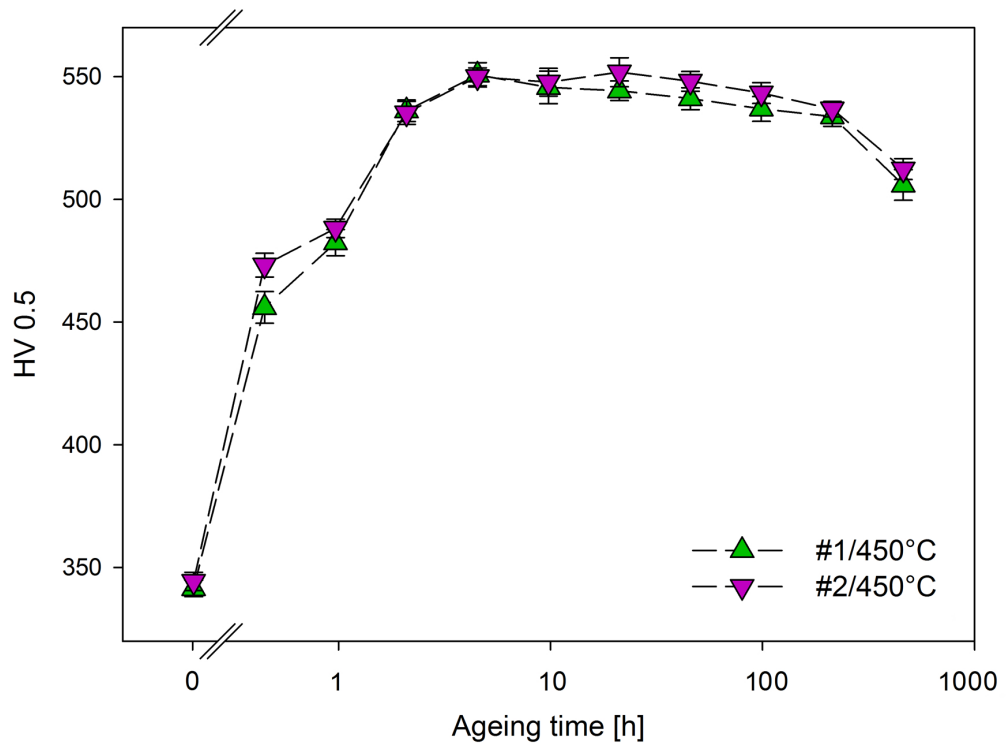


Figure 5.7: Microhardness evolution for condition 1 and 2 aged at 450 °C

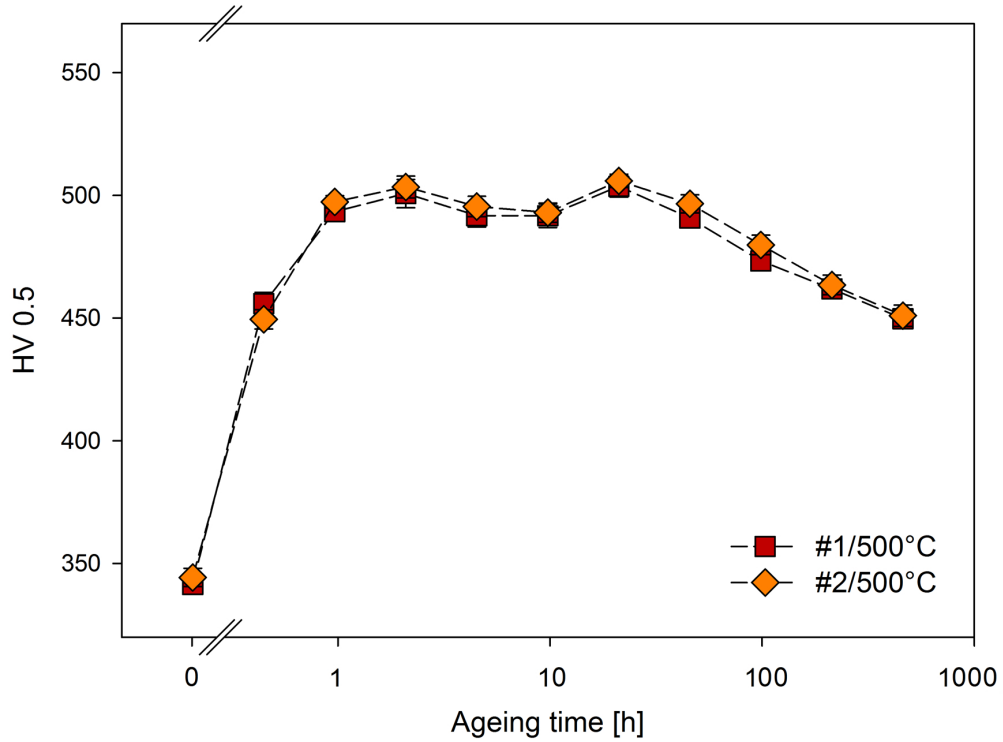


Figure 5.8: Microhardness evolution for condition 1 and 2 aged at 500 °C

500 °C. Fig. 5.5 and Table 5.1 show that the highest microhardness for samples aged at 400 °C and 450 °C is around 550 HV while for the highest ageing temperature, 500 °C, the microhardness reaches a value of 505 HV.

Based on the results obtained from microhardness measurements, sets of samples for scanning electron microscopy (SEM) and X-ray diffraction (XRD) were selected.

5.5 X-Ray Diffraction

X-Ray diffraction was measured on selected samples, primarily focusing on condition 1. As phase transformations in the material do not depend on grain boundary α characteristics (see Table 3.3), similar results from X-Ray diffraction are to be expected in condition 2. Therefore, only a few spot-checks to condition 2 were made and confirmed this assumption. Selected samples from condition 1 were the following: 0.5 h, 1 h, 2 h, 4 h, 16 h, 64 h and 256 h aged at 400 °C; 0.5 h, 1 h, 2 h, 4 h, 8 h and 16 h aged at 450 °C and finally 0.5 h, 1 h, 2 h aged at 500 °C. Only three samples from the ageing treatment at 500 °C were measured, since no ω phase was detected at this temperature. As it was mentioned before, the measurements were made using Bruker D8 Advance diffractometer equipped with rotational sample holder. The sample was rotated during signal acquisition in order to minimize the influence of texture in the material and to reduce poor statistics due to large grains. The measurements were done in 2θ angle range of

32 – 112°. The detector moved with step size of 0.025° and signal acquisition time at each angle was 54 s. Thus, the total number of steps in the line profile was 3200 and the whole spectrum was measured for 48 h. As the measurements were rather time-demanding, only a limited number of samples could be measured.

The resulting line profiles (plots of intensity versus 2θ angle) were analyzed using *MStruct*, a free computer program for microstructure analysis from powder diffraction data. The program uses a typical Rietveld method of least squares and includes physically relevant models for peak broadening and shift. The instrumental function for correction of peak broadening was also included. The program allows multiple parameters to be determined for each phase present in the alloy, e.g. lattice parameters, average crystallite sizes, volume fractions and residual stresses [47].

Analysis of the X-Ray line profiles showed that the ω phase was present in all measured samples aged at 400 °C (samples aged up to 256 h). At 450 °C, ω particles were detected up to 2 h of ageing, then they either dissolved or were too small or overlapped by secondary α phase for the system to pick up. The X-Ray diffraction showed no evidence of ω phase in samples aged at the highest ageing temperature, 500 °C.

Firstly, volume fractions of individual phases were determined by analysis of the X-Ray diffraction data. The dependence of volume fractions on ageing time is shown in Fig. 5.9, Fig. 5.10 and Fig. 5.11 for ageing temperatures of 400 °C, 450 °C and 500 °C, respectively.

At 400 °C, the ω phase volume fraction of approximately 60% after 0.5 h of ageing was determined. The volume fraction of ω phase then increases slightly at the expense of β phase whose volume fraction simultaneously decreases with increasing ageing time (see Fig. 5.9). After 4 h, a drop in volume fraction of ω phase is observed. This decrease is not entirely caused by $\omega \rightarrow \alpha$ transformation, rather, the ω phase partially reverts back to the β structure, as evidenced by an increase of β volume fraction. After 256 h of ageing, there is only about 2% of ω phase left in the sample. The volume fraction of α phase increases very slowly in the first few hours of ageing. Nevertheless, a rapid increase corresponding to growth of the α phase is observed after longer ageing times.

Fig. 5.10 shows the volume fraction evolution of each phase during ageing at 450 °C. With increasing ageing time, the volume fraction of ω phase decreases rapidly and after only 4 h no ω particles were detected any more in the studied material. In contrast to ageing at 400 °C, α phase starts to precipitate and grow very early at 450 °C (compare Figures 5.9 and 5.10). There is a major increase in its volume between samples aged for 0.5 h and 1 h. With increasing ageing time the volume fraction of α phase continuously increases. The volume fraction of β matrix first decreases at the beginning of ageing due to rapid growth of α phase. Then its volume fraction increases temporarily which indicates that the dissolution of ω phase back to β becomes dominant over α phase growth. After 4 h of ageing, only a two-phase process is observed, in which the secondary α phase particles grow at the expense of β matrix.

Finally, volume fractions of α and β phases in samples aged at 500 °C are shown in Fig. 5.11. As it was mentioned before, only three samples aged at this temperature were measured using X-Ray diffraction due to the fact that no ω phase was observed. Therefore, Fig. 5.11 demonstrates initial stages of α phase

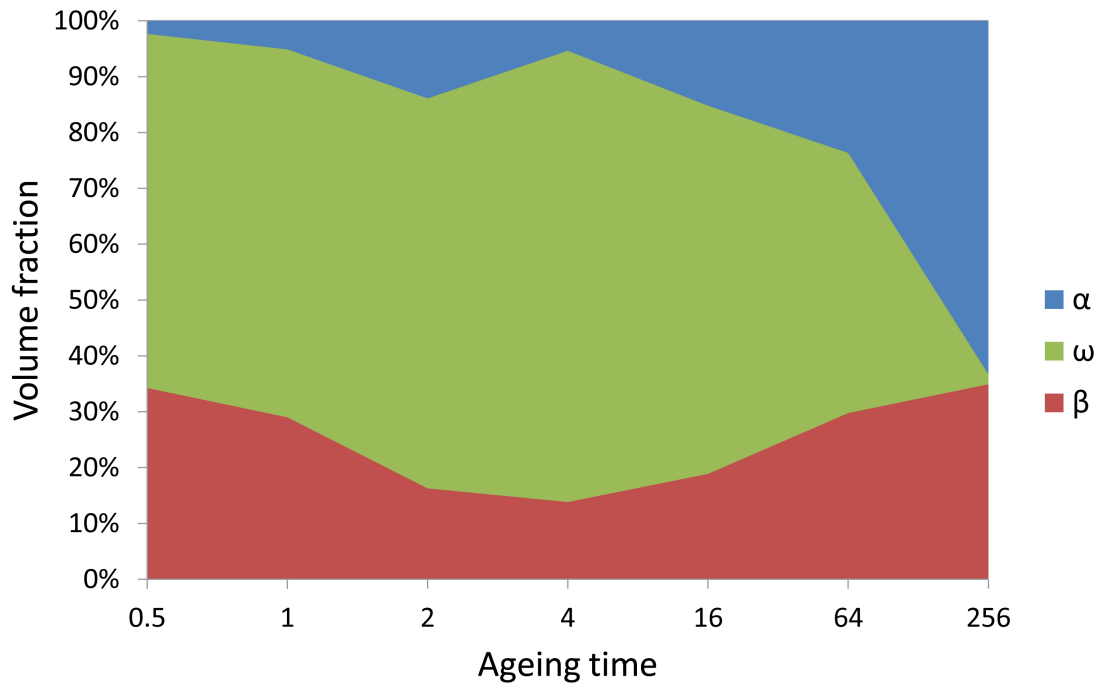


Figure 5.9: Volume fractions of α , β and ω phases in samples aged at 400 °C

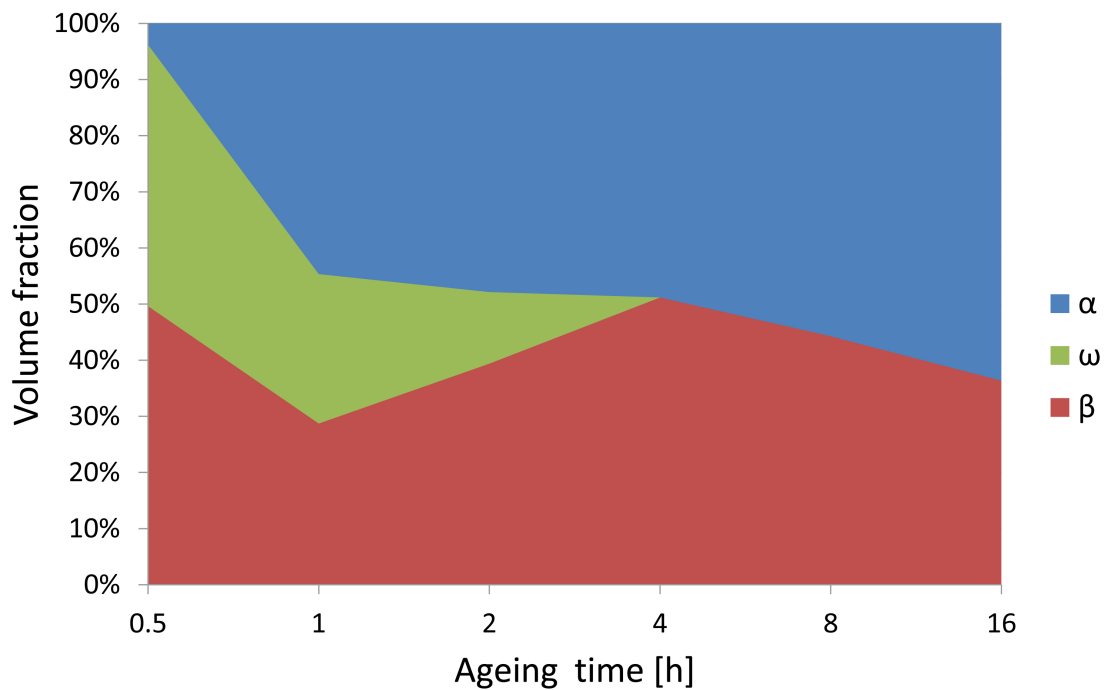


Figure 5.10: Volume fractions of α , β and ω phases in samples aged at 450 °C

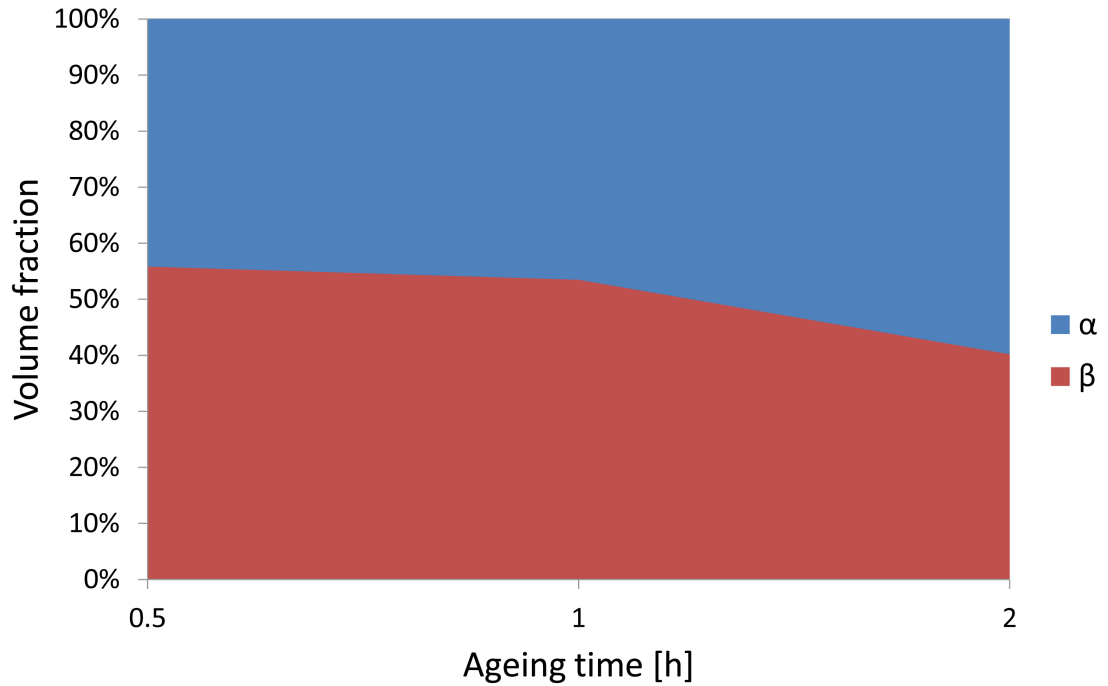


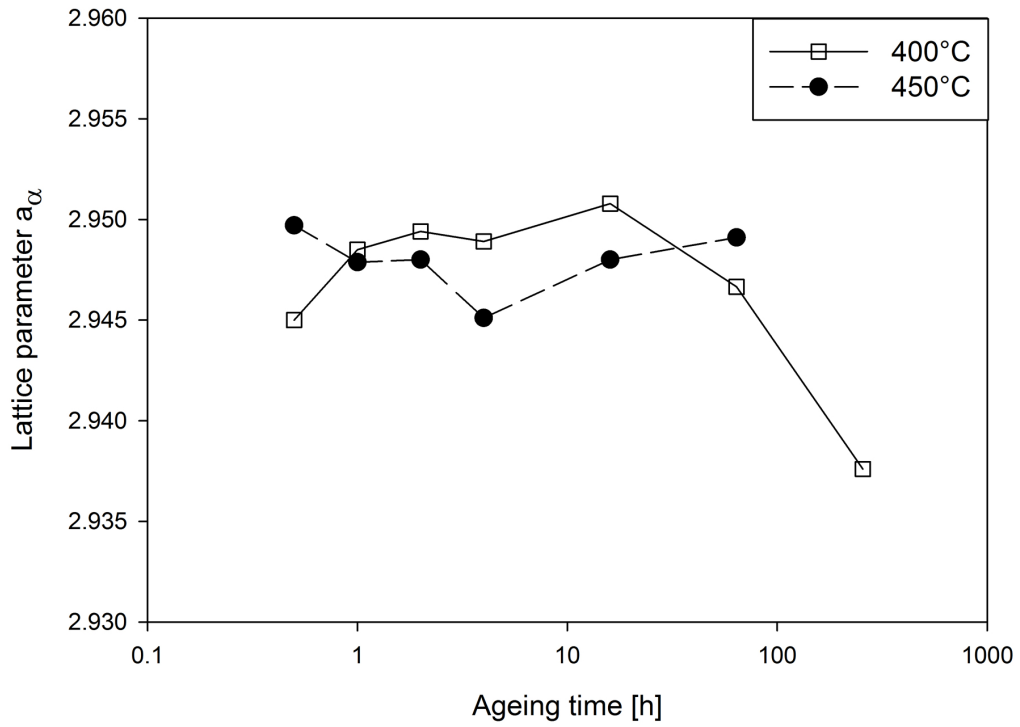
Figure 5.11: Volume fractions of α and β phases in samples aged at 500 °C

growth in β matrix.

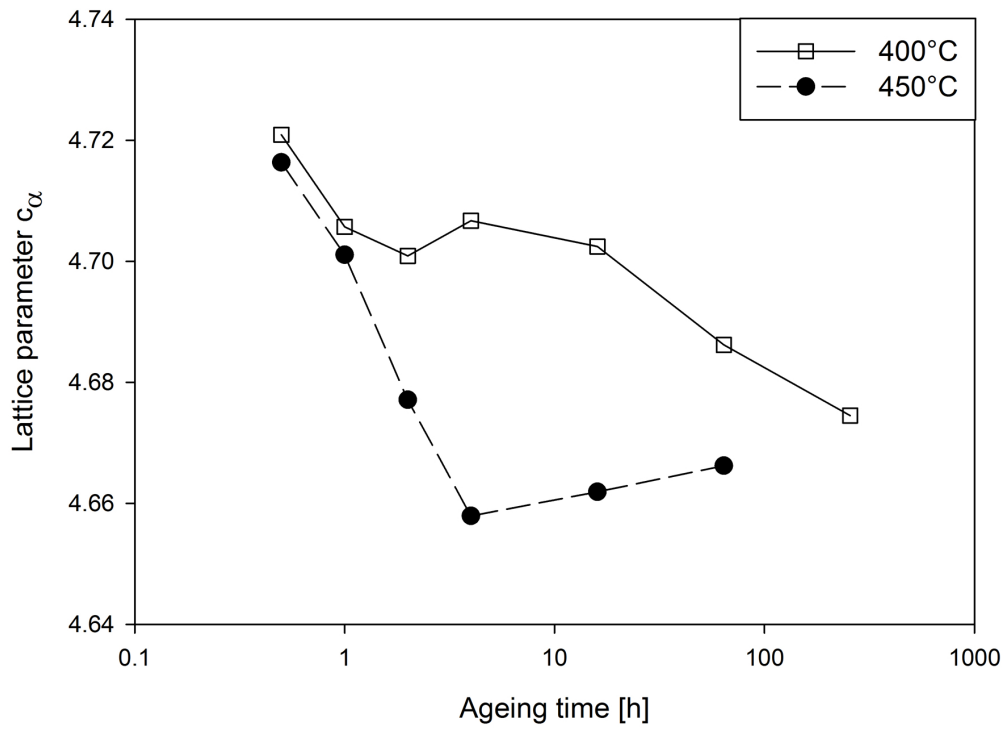
The changes of lattice parameters with increasing ageing time for each phase will be discussed next. Plots of variations in lattice parameters for α , β and ω phases are shown in Fig. 5.12a–5.12e for ageing temperatures of 400 °C and 450 °C. Lattice parameter changes for 500 °C are not plotted, since only three samples aged for the shortest times (0.5 h, 1 h and 2 h) were measured.

As indicated by Fig. 5.12a, the lattice parameter a of the hexagonal close-packed α phase (a_α) is roughly independent of time, decreasing only at the highest ageing times at 400 °C. It should be emphasized, that the accuracy of determination of α lattice parameters is rather low due to the fact that there are two different α morphologies present in the material. The first one is the primary α which precipitated at grain boundaries of the β matrix during α/β solution treatment, the second one is the secondary α phase precipitating during ageing. These two morphologies may have slightly different lattice parameters resulting in a greater dispersion of measured values. Fig 5.12b shows the evolution of lattice parameter c of α phase (c_α). This parameter tends to decrease with increasing ageing time. This decrease is most likely caused by rejection of heavier β stabilizers (Fe, Mo) from the growing α phase. The slope of the decrease is steeper for the higher ageing temperature (450 °C), which is in accordance with faster diffusion rates at higher temperatures.

Plot of lattice parameter a of the hexagonal ω phase (a_ω) against ageing time is shown in Fig. 5.12c. At 400 °C, a_ω is constant up to longer ageing times, where its value starts to drop. During ageing at 450 °C, the c_ω lattice parameter does not change significantly in the range of ageing times where ω phase was detected. On the other hand, the c_ω parameter strongly depends on the ageing time. This fact is pronounced especially at 400 °C where ω phase was present in the whole studied

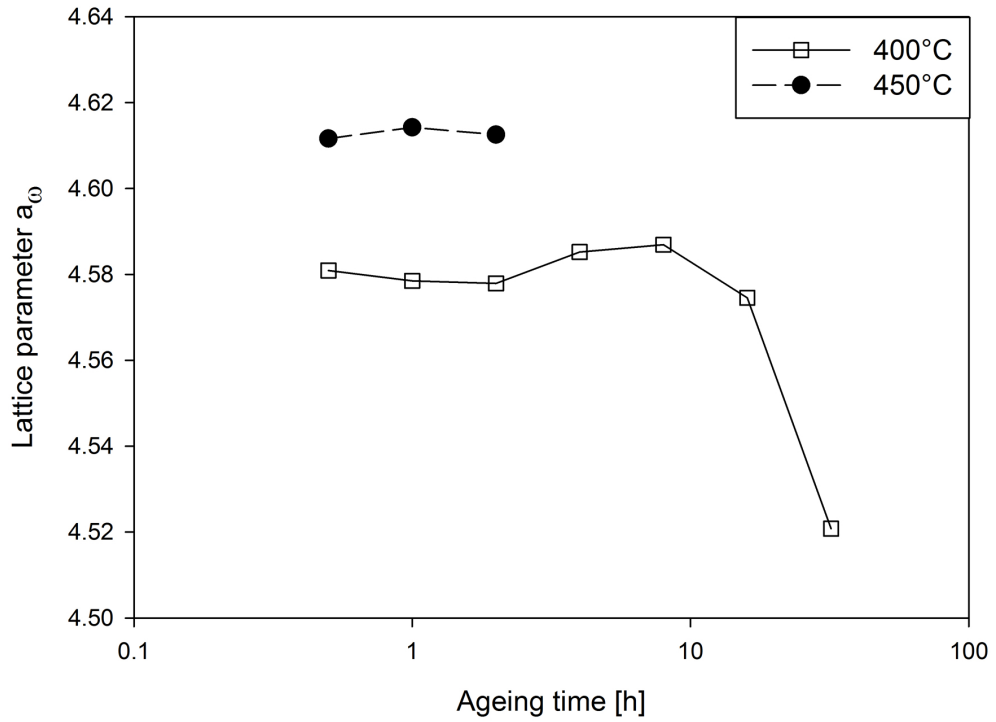


(a) a_α lattice parameter

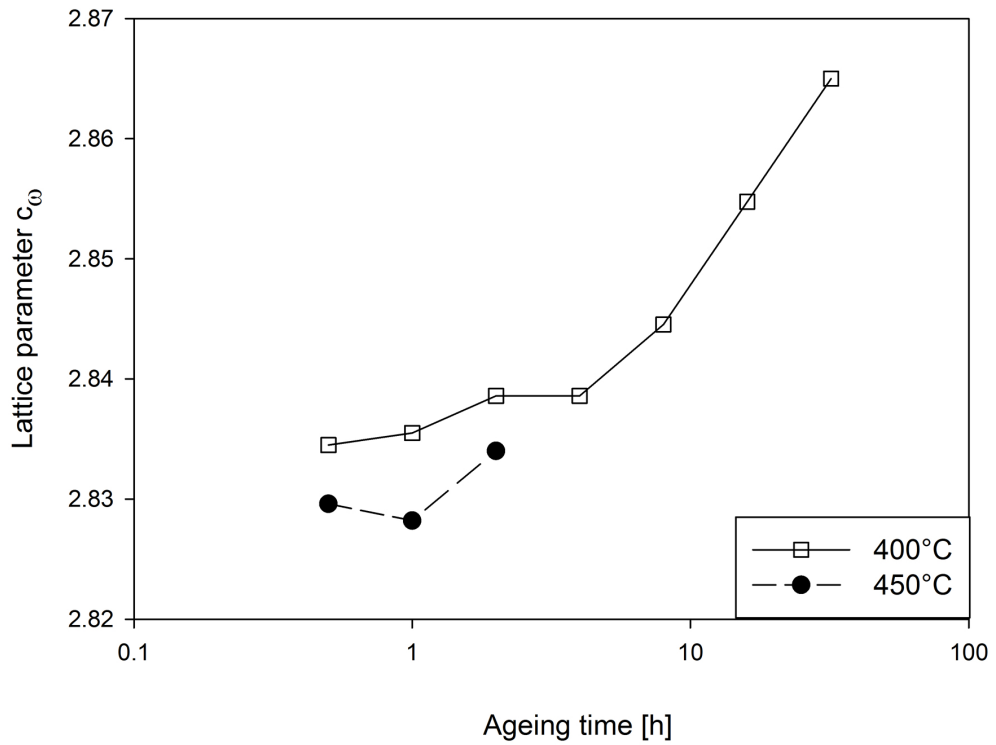


(b) c_α lattice parameter

Figure 5.12: Influence of ageing time and temperature on lattice parameters of α , β and ω phase

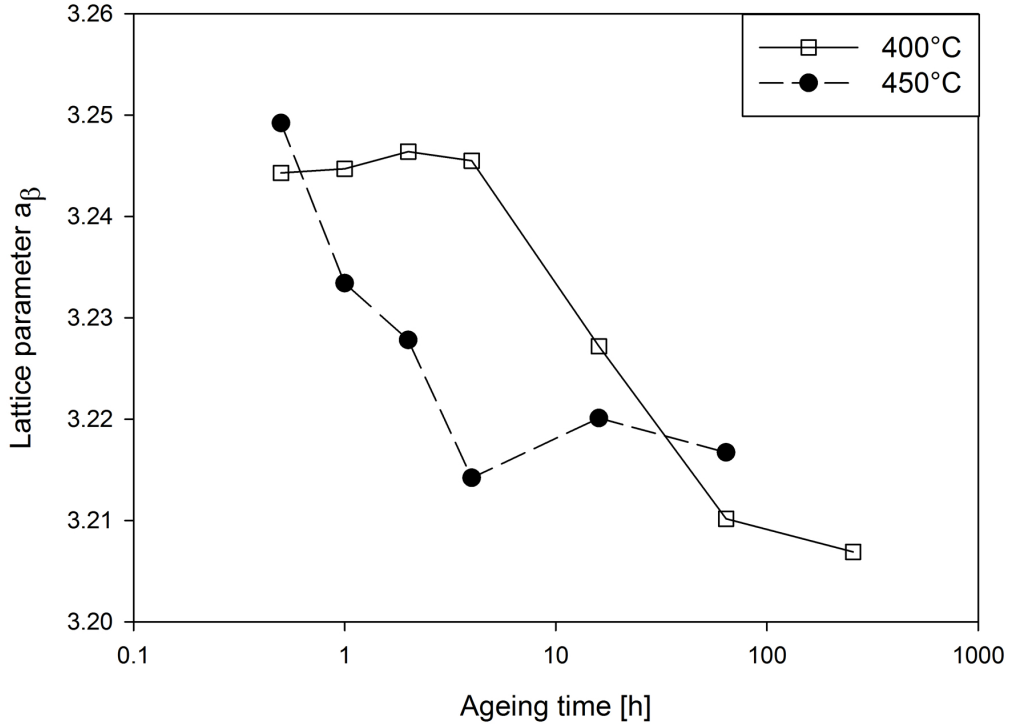


(c) a_ω lattice parameter



(d) c_ω lattice parameter

Figure 5.12: (Continued) Influence of ageing time and temperature on lattice parameters of α , β and ω phase



(e) a_β lattice parameter

Figure 5.12: (Continued) Influence of ageing time and temperature on lattice parameters of α , β and ω phase

range of ageing times. Fig. 5.12d demonstrates how the parameter increases with increasing ageing time.

Finally, the variations of lattice parameter of the body-centered β phase (a_β) will be discussed. At the lowest ageing temperature, 400 °C, the β -phase parameter is nearly constant for shorter ageing times. However, after 4 h a decrease in its value is apparent. At 450 °C the lattice parameter decreases with increasing ageing time immediately after the beginning of ageing. SEM micrographs in Section 5.6 will demonstrate that the decrease in the lattice parameter of β phase is related to nucleation and growth of secondary intragranular α phase.

5.6 Scanning electron microscopy

Scanning electron microscopy (SEM) was used to observe both initial α/β solution treated conditions of the material as well as multiple selected aged samples. Samples aged at 400 °C, 450 °C and 500 °C for 0.5 h, 4 h, 32 h and 256 h were chosen for this study. All SEM images shown in this chapter are in back-scattered electron contrast mode.

As it was stated before (Section 2.4), secondary α phase precipitates within the β matrix during ageing of the material. The evolution of the microstructure during ageing is demonstrated in following figures and accompanying discussion.

First, we will focus on microstructural changes during ageing at the lowest

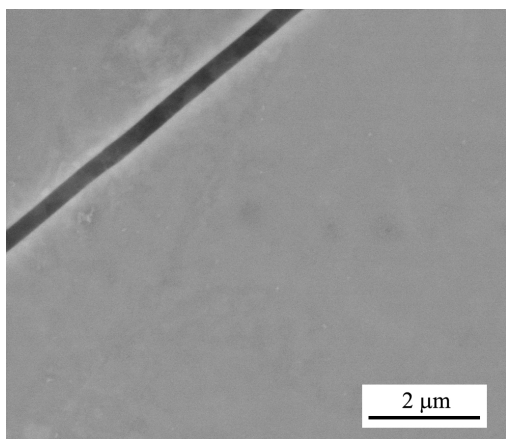


Figure 5.13: Condition 1, aged at 400 °C for 0.5 h

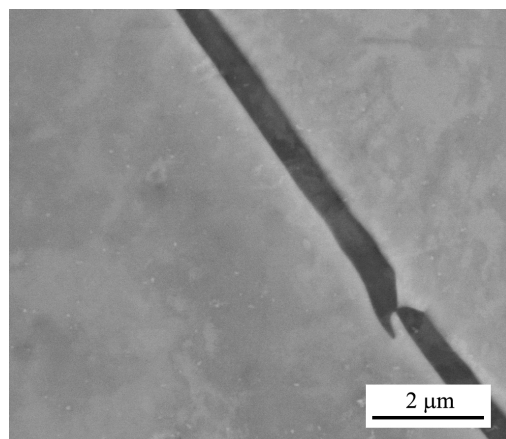


Figure 5.14: Condition 2, aged at 400 °C for 0.5 h

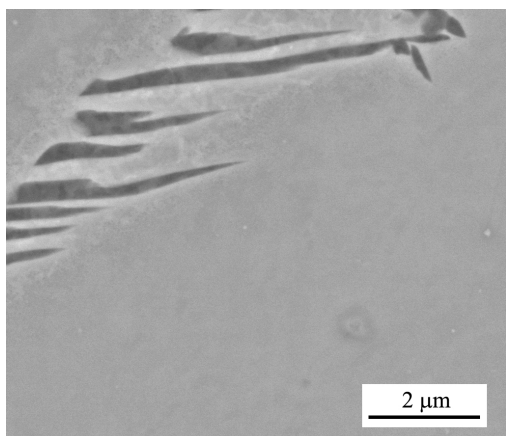


Figure 5.15: Condition 1, aged at 400 °C for 4 h

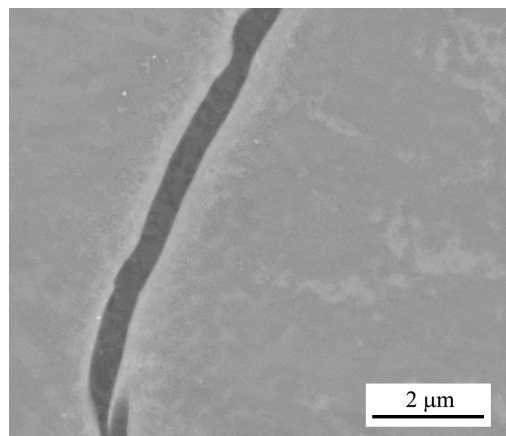


Figure 5.16: Condition 2, aged at 400 °C for 4 h

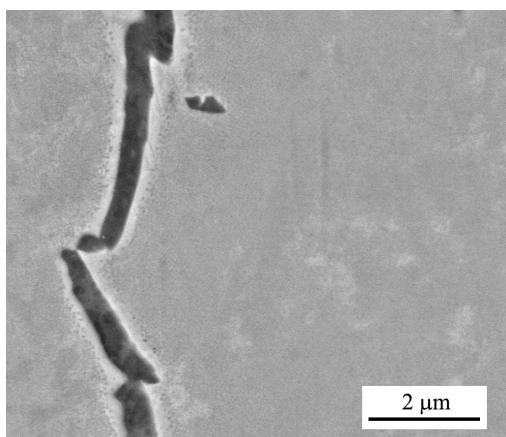


Figure 5.17: Condition 1, aged at 400 °C for 32 h

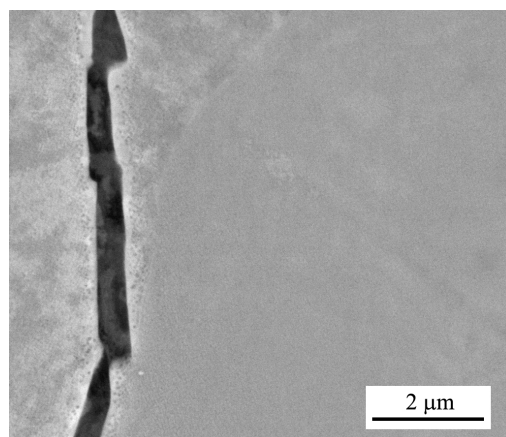


Figure 5.18: Condition 2, aged at 400 °C for 32 h

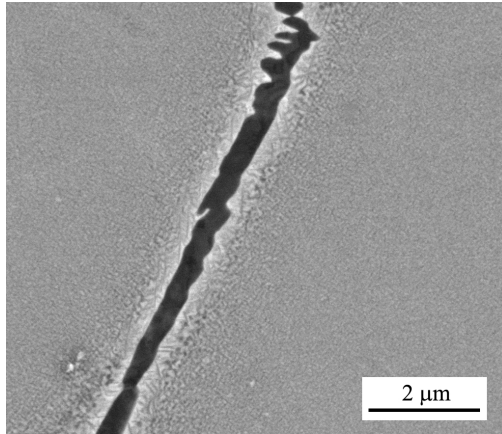


Figure 5.19: Condition 1, aged at 400 °C for 256 h

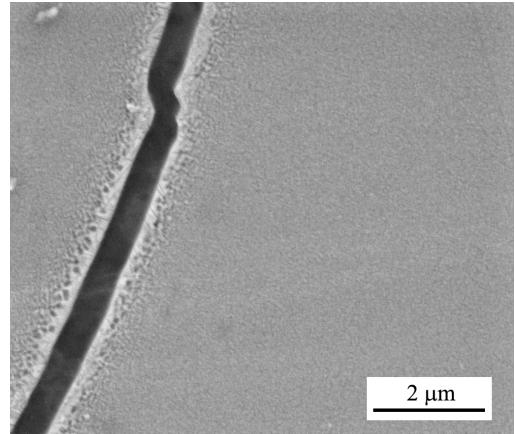


Figure 5.20: Condition 2, aged at 400 °C for 256 h

studied temperature, 400 °C. Samples aged at this temperature for 0.5 h, 4 h, 32 h and 256 h are shown in Figures 5.13, 5.15, 5.17 and 5.19 for condition 1 and in Figures 5.14, 5.16, 5.18 and 5.20 for condition 2. At early stages of ageing at the lowest temperature (for example 0.5 h in Fig 5.13 or 5.14), no α precipitation was observed. With increasing ageing time, α phase starts to precipitate at a certain distance from primary grain boundary α . These small α particles appear as tiny dots of darker grey in Figures 5.15 and 5.16 (samples of both conditions aged for 4 h). This process is further pronounced after 32 h of ageing (see Figures 5.17 and 5.18) where growing particles of α phase are evident. In direct proximity of the grain boundary α film precipitate-free zones form. Precipitate-free zone is an area where the nucleation of α phase is suppressed due to higher concentration of β stabilizing elements which were rejected during the heterogeneous nucleation and growth of grain boundary α phase. As the β stabilizing elements Mo and Fe have higher atomic number than α stabilizer Al, bright regions adjacent to the primary α are observed in back-scattered contrast images. After ageing at 400 °C for the longest ageing time (256 h), α precipitates can be observed in the whole volume of β grain (Fig. 5.19 and 5.20). This intragranular α phase has a very fine equiaxed morphology and is evenly distributed throughout the interior of the β grains. The fine dispersion of α particles indicates that it nucleated in one of the ω assisted ways mentioned in Section 2.4.3. Closer examination of regions adjacent to grain boundary α revealed that secondary α starts to precipitate even in the former precipitate-free zones. This α phase exhibits elongated, lamellar microstructure. This different morphology in the vicinity of primary grain boundary α phase is most likely caused by fewer ω particles present in this β stabilizer enriched region. Since particles of ω phase serve as heterogeneous nucleation sites for α phase, the precipitated α particles are distributed sparsely and thus can elongate more before they impinge on the adjacent ones. Compared to the results of microhardness measurement (see Fig. 5.5), it is apparent that these fine, evenly distributed particles of α phase are connected with the highest value of hardness.

The comparison of images for condition 1 and 2 for each ageing time indicates that the microstructure of both conditions evolves similarly during ageing treatment. Therefore, different α/β solution treatments resulting in different

grain boundary α characteristics have no influence on ageing properties of the material.

At higher ageing temperature, 450 °C, the rate of occurring phase transformations is higher due to higher mobility of solute atoms. The onset of secondary α formation is also earlier. Even after the shortest ageing time (0.5 h, see Fig. 5.21 for condition 1 and Fig. 5.22 for condition 2), the α phase precipitated inside the β matrix. The morphology of this intragranular α phase can be characterized as finely dispersed equiaxed particles, which is very similar to the character of α observed during ageing at 400 °C. Precipitation-free zones appear in the vicinity of grain boundary α similarly as at 400 °C. With increasing ageing time, the secondary α particles coarsen (Fig. 5.23 and 5.24). Furthermore, after 32 h of ageing shown in Figures 5.25 and 5.26, fine lamellar α precipitates can be found directly adjacent to the grain boundary α phase. It is evident from the two above mentioned images that these α platelets grow only in certain directions in respect to the crystallographic orientation of β matrix. Their orientation is determined by Burgers relationship between the α and β phase, the exact relationship being expressed in equation 2.7 in Section 2.4.2. Finally, after ageing at 450 °C for 256 h the particles of secondary α phase become much coarser in the interior of β grains as well as near the grain boundary α film. It should be noticed that the morphologies of intragranular α and the α phase precipitated adjacent to grain boundaries are quite different. Whereas the precipitates adjacent to the primary α phase grow in long, needle-like structure protruding inside the β grains, the intragranular α can be characterized as spheroidal with decreased length to width ratio. This fact could be explained by more α nuclei forming inside the β grains than in the proximity of grain boundary α where the precipitation is limited due to higher β stabilizer content. Higher density of α nuclei in the interior of β grains provides less space for the α plates to grow freely. This results in earlier impingement of α particles and their spheroidal shape. The comparison to microhardness results for ageing temperature of 450 °C in Fig. 5.7 indicates that the highest strength of the material (after 4 h of ageing treatment) corresponds to the microstructure shown in Fig. 5.23 and 5.24. After 256 h (see Fig. 5.27 and 5.28) the resulting microstructure is overaged, as evidenced by a rapid decrease in microhardness in Fig. 5.7.

Finally, the highest ageing temperature of 500 °C will be discussed. Corresponding images of microstructure evolution are shown in Figures 5.29, 5.31, 5.33 and 5.35 for condition 1 and in Figures 5.30, 5.32, 5.34 and 5.36 for condition 2. During heat treatments at this temperature, α plates form very quickly in the material. Already after 30 min (see Fig. 5.29 for condition 1 or Fig. 5.30 for condition 2), fully developed secondary α plates are observed within the β grains. In contrast to equiaxed morphology of intragranular α phase found in samples aged at lower temperatures (400 °C and 450 °C), α particles precipitated at 500 °C can be characterized as needle-like. The needle-like shape can be explained by instability of ω phase formed during quenching of the alloy and its quick dissolution at this temperature. Therefore, fewer ω particles are able to serve as nucleation sites for α phase precipitation during the first 30 min of ageing. As it was reported by other authors [30], α phase formation at 500 °C may not be ω assisted at all. Instead, homogeneous nucleation of α phase in the β matrix takes place. As a consequence, the distribution of nucleated α phase is more sparse

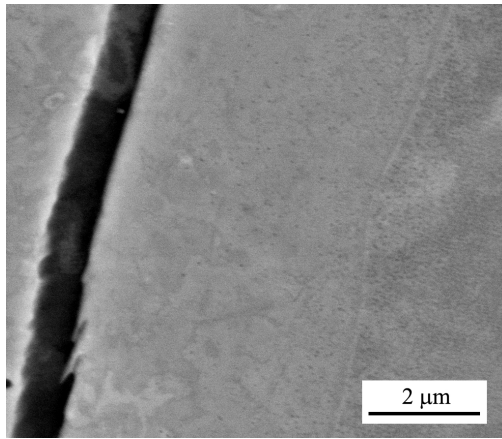


Figure 5.21: Condition 1, aged at 450 °C for 0.5 h

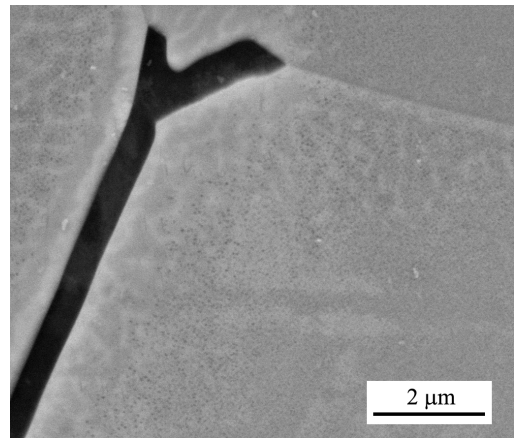


Figure 5.22: Condition 2, aged at 450 °C for 0.5 h

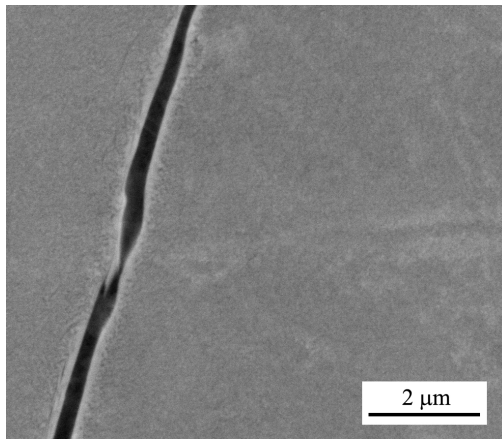


Figure 5.23: Condition 1, aged at 450 °C for 4 h

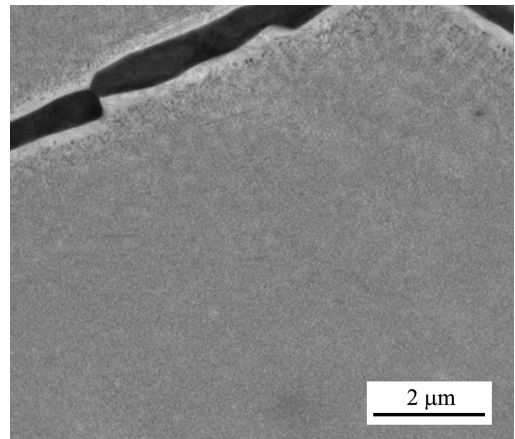


Figure 5.24: Condition 2, aged at 450 °C for 4 h

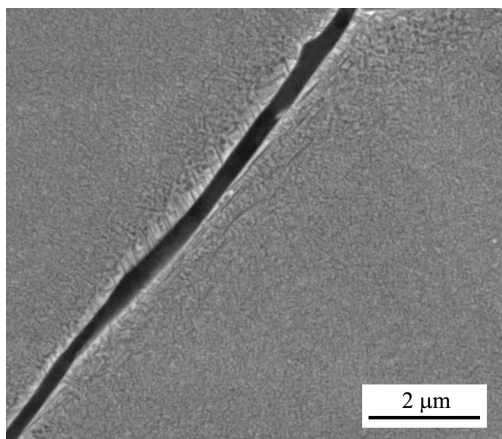


Figure 5.25: Condition 1, aged at 450 °C for 32 h

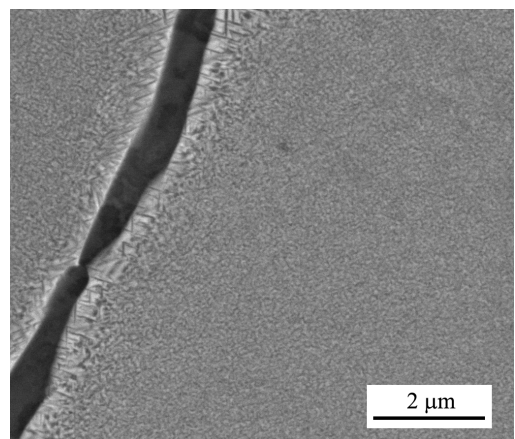


Figure 5.26: Condition 2, aged at 450 °C for 32 h

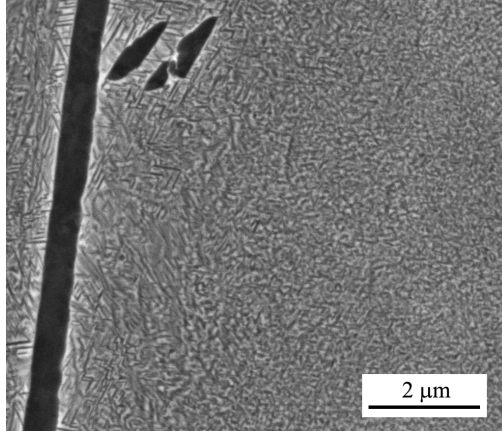


Figure 5.27: Condition 1, aged at 450 °C for 256 h

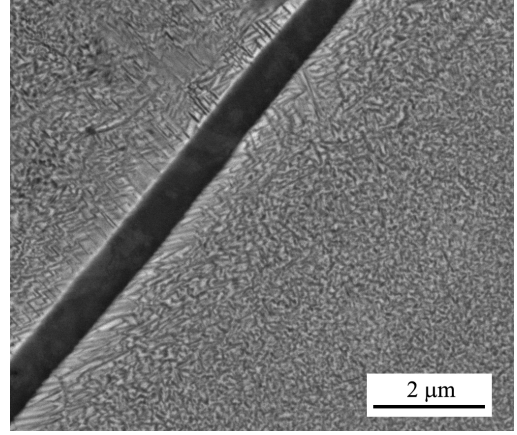


Figure 5.28: Condition 2, aged at 450 °C for 256 h

and thus the plates can elongate more before they impinge on the adjacent ones. As evidenced by images showing the microstructure of the material after 4 h of ageing (see Figures 5.31 and 5.32), the precipitate-free zone disappeared much sooner than at the lower ageing temperature. While secondary α plates adjacent to grain boundary α were observed after 256 h or 32 h at 400 °C or 450 °C, respectively, the α phase formation in precipitate-free zones started already in the first 4 h of ageing at 500 °C. With increasing ageing time, secondary α platelets coarsen, both in grain interiors and near the grain boundary α (see Figures 5.33 and 5.34 for condition 1 and 2 aged for 32 h). Finally, the longest ageing time (256 h) at 500 °C resulted in very large and thick plates of secondary α phase. As the microhardness results in Fig. 5.8 indicate, samples aged for more than 32 h (microstructures shown in Fig. 5.33, 5.34, 5.35 and 5.36) are overaged, i.e. their hardness is reduced.

In order to verify the chemical composition of the alloy TIMETAL LCB, local analysis was done using energy dispersive X-Ray spectroscopy (EDS). Average elemental composition was determined from a larger area of surface of an unaged sample. The accelerating voltage used for this experiment was 20 keV. The resulting values for each element in weight and atomic percents are listed in Table 5.2 along with the standard chemical composition of TIMETAL LCB given by the manufacturer of the alloy. As can be seen, these values are in good agreement. The measured EDS spectrum is shown in Fig. 5.37.

Element		Ti	Mo	Fe	Al
Wt. %	EDS	86.4	7.3	4.6	1.7
	Nominal	87.2	6.8	4.5	1.5
At. %	EDS	89.1	3.7	4.0	3.2
	Nominal	89.8	3.5	4.0	2.7

Table 5.2: Average chemical composition of TIMETAL LCB determined by EDS and its comparison with nominal values

Furthermore, chemical analysis of primary α precipitates at grain boundaries was also performed. Due to small sizes of these precipitates, lower accelerating

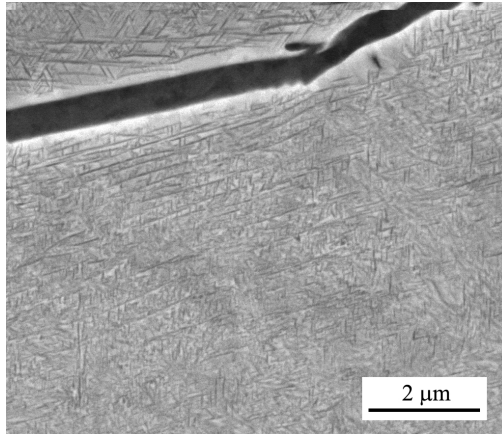


Figure 5.29: Condition 1, aged at 500 °C for 0.5 h

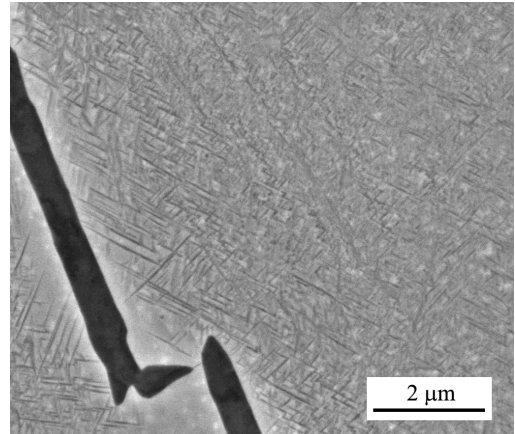


Figure 5.30: Condition 2, aged at 500 °C for 0.5 h

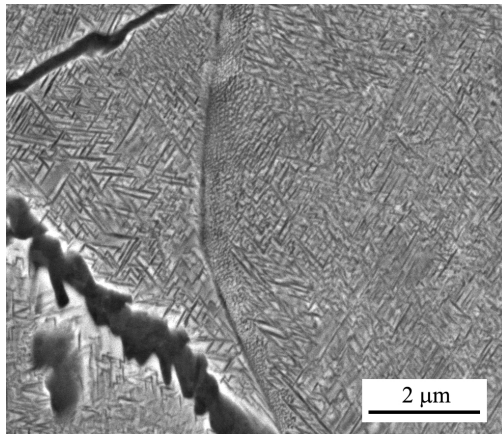


Figure 5.31: Condition 1, aged at 500 °C for 4 h

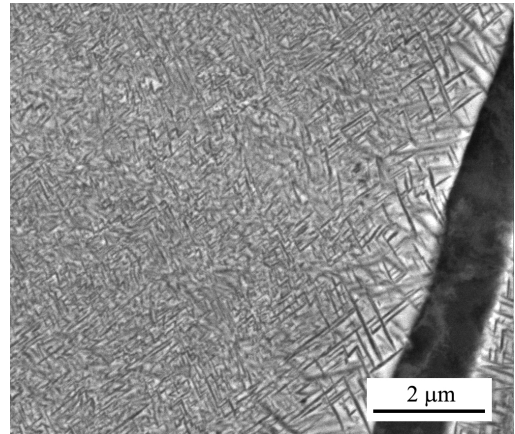


Figure 5.32: Condition 2, aged at 500 °C for 4 h

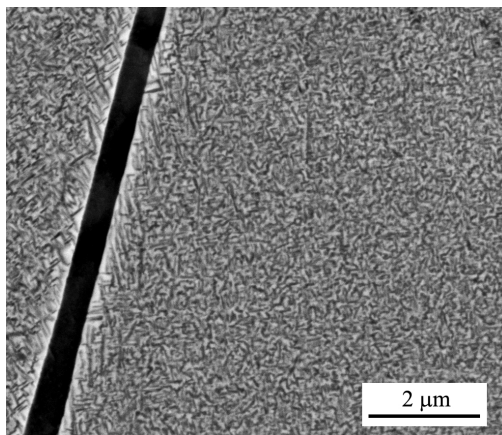


Figure 5.33: Condition 1, aged at 500 °C for 32 h

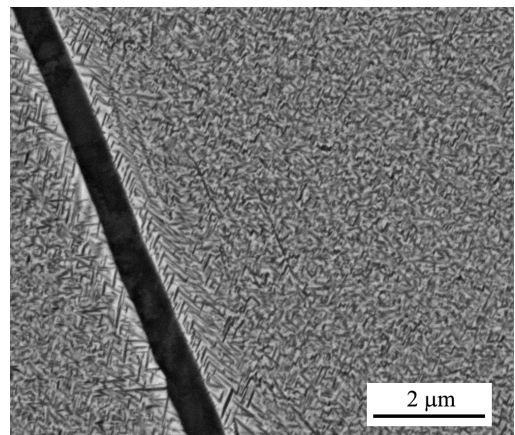


Figure 5.34: Condition 2, aged at 500 °C for 32 h

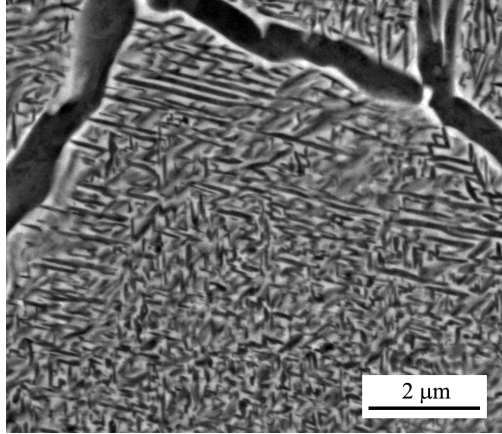


Figure 5.35: Condition 1, aged at 500 °C for 256 h

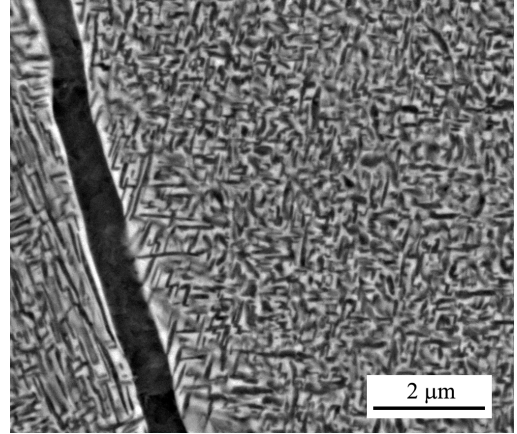


Figure 5.36: Condition 2, aged at 500 °C for 256 h

voltage (10 keV) was used. Lower accelerating voltage reduced the interaction volume and thus limited the possibility of detecting the interfering signal from β grains surrounding the grain boundary α phase. The results of this analysis, which are summarized in Table 5.3 and Fig. 5.38, confirm that the α stabilizer (Al) diffuses into the grain boundary α film and β stabilizing elements (Fe, Mo) are rejected from it. No iron was detected in the primary α phase at all. The lower concentration of heavier elements Fe and Mo in the α phase also explains the contrast formation between α (darker) and β phase (lighter shade) in back-scattered electron signal.

Element	Ti	Mo	Fe	Al
Wt. %	95.1	2.4	0.0	2.5
At. %	94.4	1.2	0.0	4.4

Table 5.3: Average chemical composition of grain boundary α phase determined by EDS

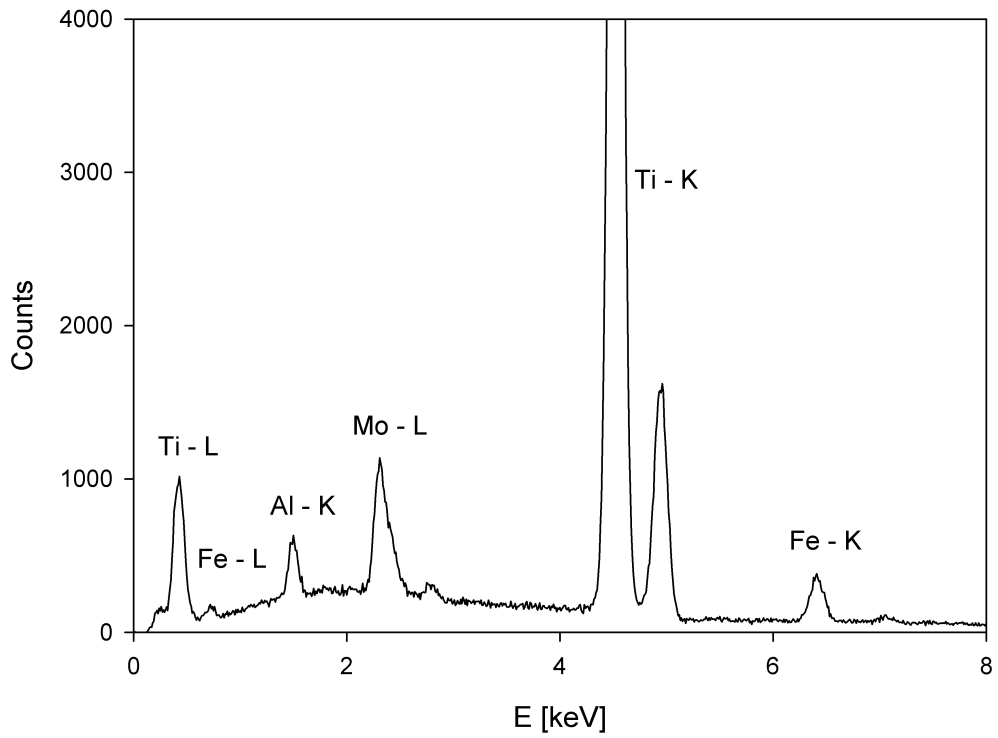


Figure 5.37: EDS spectrum taken from a larger area of the sample

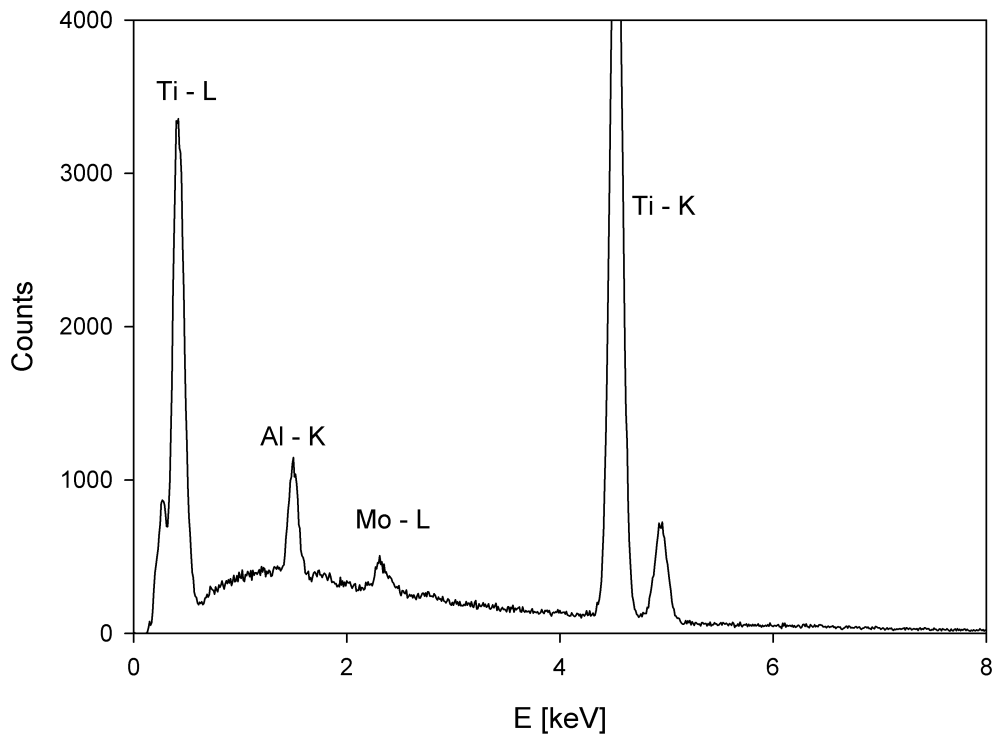


Figure 5.38: EDS spectrum of grain boundary α phase

5.7 Tensile testing

For tensile tests, four heat treated conditions were selected both from condition 1 and condition 2, in particular the specimens aged for 8 and 16 h at 450 °C and 500 °C. These aged conditions were selected based on the results of microhardness and X-ray measurements. These samples exhibited high values of microhardness, while the analysis of X-ray spectra indicated that there is either none or very little ω phase left in the material. Greater amounts of ω particles are expected to result in embrittlement of the alloy. The tensile tests were performed at room temperature with the strain rate of 10^{-4} s^{-1} . The results are summarized in Table 5.4. The table lists the values of ultimate tensile strength (UTS), elongation, yield stress and plastic strain for each tested sample. As all measured samples exhibited very low ductility, no necking and subsequent decrease in engineering stress–strain curve was observed. Therefore, the ultimate tensile strength corresponds to the fracture stress. The elongation was measured by a video extensometer during the sample loading. It is therefore the total elongation which includes plastic as well as elastic deformation. The values of engineering yield

Cond.	Temperature [°C]	Time [h]	UTS [MPa]	Elongation [%]	$\sigma_{0.2}$	ε_p
1	450	8	1403	1.4	N/A	0.00
		16	1280	1.2	N/A	0.00
	500	8	1527	1.9	1507	0.32
		16	1507	1.9	1482	0.41
2	450	8	1493	1.6	1470	0.30
		16	1275	1.2	N/A	0.00
	500	8	1523	1.7	1505	0.30
		16	1514	2.0	1468	0.63

Table 5.4: Tensile properties – ultimate tensile strength (UTS), elongation, yield stress ($\sigma_{0.2}$) and plastic strain (ε_p)

stress ($\sigma_{0.2}$) and plastic strain (ε_p) in Table 5.4 were automatically evaluated by the tensile machine software. Since the elastic strain (ε_{el}) disappears after the applied stress is removed, the plastic strain can be expressed as $\varepsilon_p = \varepsilon - \varepsilon_{el}$, where ε is the total strain observed while the sample is loaded. Some of the samples fractured already during the elastic deformation, thus they had no plastic strain and the yield stress could not be calculated, which is indicated by N/A in the $\sigma_{0.2}$ cells of Table 5.4.

It is worth mentioning that correct Young’s modulus is obtained from the measured values of stress and strain. When the elastic strain is calculated by subtraction of ε_p from elongation for each row in Table 5.4, the average of $(1.4 \pm 0.1) \%$ is obtained. The Young’s modulus, derived according to Hooke’s law in Equation 3.8 by dividing the yield stress by the average elastic strain, is then 100 – 110 GPa. This value is in a good accordance with Young’s modulus given in technical reports on TIMETAL LCB (110 – 117 GPa, see Table 3.1).

The results of the tensile tests show that conditions 1 and 2 have very similar tensile properties and the material exhibits very high strength in all aged conditions. At 450 °C overall lower values of ultimate tensile strength (UTS) are observed compared to the samples aged at 500 °C. Furthermore, the material aged at 450 °C exhibited brittle behaviour and often fractured already in the elastic region of the stress–strain curve as evidenced by Table 5.4. This fact could be

attributed to some ω phase still present in the samples aged at 450 °C. Since no ω phase was observed in these heat treated conditions by X-ray diffraction, this would mean the ω particles are either too small or have too low volume fraction to be detected by the X-ray diffraction. This explanation is supported by the fact that at this temperature (450 °C), higher ultimate tensile strength was observed in samples aged for 8 h (1403 and 1493 for conditions 1 and 2, respectively, compared to the respective values of 1280 and 1275 for conditions 1 and 2 aged for 16 h). This would correspond to dissolution of ω particles after longer ageing times and resulting lower tensile strength. At 500 °C, approximately the same values of ultimate tensile strength (UTS in Table 5.4) as well as yield stress ($\sigma_{0.2}$ in Table 5.4) are observed in samples aged for 8 h and 16 h.

Unexpectedly low values of plastic strain and corresponding low ductility were observed in all the tested samples. Even in those heat treated conditions in which ω phase was neither measured nor expected (e.g. aged at 500 °C for 16 h), the elongation reached only 2 %. This embrittlement of the material can be hardly attributed to α precipitates within the β matrix. Since the ultimate goal of the ongoing research is to prove the influence of α/β solution treatment on fatigue properties of the material, higher values of ductility, e.g. 5 % and more, would be needed to perform the fatigue tests. Therefore, any undesirable effects such as insufficient cooling during the machining of the tensile samples or flaws in the surface finishing will have to be ruled out first and the tensile tests re-done before time and material consuming fatigue experiments will be started.

6. Conclusions

The focus of the present work was to characterize the relationships between the evolution of phase composition during ageing and mechanical properties of TIMET LCB titanium alloy. The two initial conditions were prepared by two different α/β ageing treatments which led to precipitation of primary α along β/β grain boundaries. Both initial conditions had the same volume fraction of the grain boundary α phase, however, they differed in the contiguity and the average thickness of this α film.

The main results of the present work can be summarized as follows:

- The initial insight in the phase transformations occurring in the studied alloy during heating was obtained by differential scanning calorimetry and resistivity measurements. It was shown that at the early stages of the heat-up, athermal ω which was formed during quenching dissolved reversibly. At higher temperatures, isothermal ω grew by a diffusional irreversible process. Subsequently, ω assisted nucleation of α particles and dissolution of ω phase occurred. Finally, the $\beta \rightarrow \alpha$ transformation was observed as well as the β -transus at approximately 780 °C.
- Microhardness measurements were done to characterize the evolution of mechanical properties accompanying the ongoing phase transformations during isothermal annealing. The highest values of microhardness were reached in samples aged for 400 °C and 450 °C after 256 h and 8 h, respectively. The shift of the maximum of microhardness towards shorter ageing times with increasing ageing temperature indicated that the onset of the phase transformations (ω phase formation and α phase precipitation) leading to higher hardness of the material occurred sooner at higher ageing temperatures.
- The analysis of X-ray line profiles showed the presence of ω phase in all studied samples aged at the lowest temperature (400 °C) up to the longest ageing times. A quick dissolution of ω particles at 450 °C was observed. No ω phase was evidenced in the material aged at 500 °C. Dissolution of ω phase particles back to β matrix that accompanies the early stages of α precipitation has been proven. This is in accordance with the results of resistivity measurements.
- The results obtained from scanning electron microscopy showed that different secondary α phase morphologies formed in the material during ageing. At the lowest ageing temperature (400 °C) very fine, equiaxed and evenly distributed particles of α phase started to precipitate after 4 h of ageing treatment. The fine dispersion indicated the precipitation of α phase was ω assisted. At 450 °C, similar character of intragranular α phase was observed. Moreover, lamellar α particles became evident in the former precipitate-free zones adjacent to the primary α phase at the grain boundaries. At 500 °C, α particles with higher aspect ratio precipitated in the material. The distribution of these α particles was more sparse and they were much coarser in nature.

- Tensile tests performed on selected conditions indicated that the aged material reaches high values of strength, however, the ductility is very low which is an obvious drawback in future fatigue properties measurements.

The future work on the ongoing research will include transmission electron microscopy which will allow to characterize especially the early stages of ageing and will determine the exact size and aspect ratio of ω particles and the evolution of these parameters during heat treatment. As it was mentioned earlier, fatigue tests will be done on the conditions for which tensile testing was performed. However, the low ductility will have to be explained first and any unintended influences (e.g. during tensile sample machining) will have to be eliminated. Fatigue tests are expected to show the difference between conditions with different morphology of grain boundary α phase, since grain boundaries are known to be the preference fatigue crack initiation sites. Moreover, over 50 different heat treated conditions were already prepared for small angle X-ray scattering (SAXS) and just recently measured at Advanced Photon Source (APS) in Argonne National Laboratory in Illinois, USA. The rather complex and time demanding analysis of the results obtained by this novel research will provide a thorough understanding of ω phase precipitation, growth, distribution in β matrix, etc.

Bibliography

- [1] Wikipedia. Titanium — wikipedia, the free encyclopedia, 2012. [Online; accessed 21-March-2012].
- [2] S. Nag. *Influence of beta instabilities on the early stages of nucleation and growth of alpha in beta titanium alloys*. PhD thesis, The Ohio State University, 2008.
- [3] I. J. Polmear. *Light alloys: from traditional alloys to nanocrystals*. Butterworth-Heinemann, 2006.
- [4] G. Lütjering and J.C. Williams. *Titanium*. Springer Verlag, 2007.
- [5] C. Leyens and M. Peters. *Titanium and titanium alloys*. Wiley-VCH, 2003.
- [6] E. W. Collings. *Materials properties handbook: titanium alloys*. Asm Intl, 1994.
- [7] P. J. Bania. Beta titanium alloys and their role in the titanium industry. *JOM Journal of the Minerals, Metals and Materials Society*, 46(7):16–19, 1994.
- [8] S. Banerjee and P. Mukhopadhyay. *Phase transformations: examples from titanium and zirconium alloys*. Elsevier Science, 2007.
- [9] P. D. Frost, W. M. Parris, L. L. Hirsch, J. R. Doig, and C. M. Schwartz. Isothermal transformation of titanium-chromium alloys. *Trans. Am. Soc. Metals*, 46:231, 1954.
- [10] B. S. Hickman. The formation of omega phase in titanium and zirconium alloys: A review. *Journal of Materials Science*, 4(6):554–563, 1969.
- [11] D. De Fontaine, N. E. Paton, and J. C. Williams. The omega phase transformation in titanium alloys as an example of displacement controlled reactions. *Acta Metallurgica*, 19(11):1153–1162, 1971.
- [12] T. W. Duerig, G. T. Terlinde, and J. C. Williams. The omega-phase reaction in titanium alloys. *Titanium '80: Science and Technology*, pages 1299–1305, 1980.
- [13] Y. A. Bagaryatskiy, T. V. Tagunova, and G. I. Nosova. *Problemy metallove-deniya i fiziki metallov (Problems of Metallography and Metal Physics)*, 5, 1958.
- [14] F. R. Brotzen, E. L. Harmon Jr, and A. R. Troiano. Decomposition of beta titanium. *J. Metals*, 7, 1955.
- [15] J. M. Silcock, M. H. Davies, and M. K. Hardy. The mechanism of phase transformations in solids. *A symposium, Monograph and Report Series No. 18*, 1956.

- [16] Y. A. Bagaryatskiy, G. I. Nosova, and T. V. Tagunova. The crystallographic structure and nature of the ω -phase in titanium alloys with chromium. *Doklady Akademii Nauk SSSR*, 32:1225–1228, 1955.
- [17] E. W. Collings. *The physical metallurgy of titanium alloys*. American Society for Metals, 1984.
- [18] M. J. Blackburn and J. C. Williams. Phase transformations in Ti–Mo and Ti–V alloys. *Transactions of the Metallurgical Society of AIME*, 242, 1968.
- [19] J. C. Williams and M. J. Blackburn. The influence of misfit on the morphology and stability of the omega phase in titanium–transition metal alloys. *Transactions of the Metallurgical Society of AIME*, 245, 1969.
- [20] D. A. Porter and K. E. Easterling. *Phase Transformations in Metals and Alloys*. Chapman & Hall, 1st edition, 1981.
- [21] J. C. Williams. Critical review – kinetics and phase transformations. *Titanium science and technology*, 1973.
- [22] M. J. Donachie. *Titanium: a technical guide*. Asm Intl, 2000.
- [23] T. W. Duerig and J. C. Williams. Overview: microstructure and properties of beta titanium alloys. *Beta Titanium Alloys in the 1980's*, pages 19–67, 1983.
- [24] J. M. Silcock. An x-ray examination of the ω phase in Ti–V, Ti–Mo and Ti–Cr alloys. *Acta Metallurgica*, 6(7):481–493, 1958.
- [25] D. De Fontaine. Simple models for the omega phase transformation. *Metallurgical and Materials Transactions A*, 19(2):169–175, 1988.
- [26] D. De Fontaine. Mechanical instabilities in the bcc lattice and the beta to omega phase transformation. *Acta Metallurgica*, 18(2):275–279, 1970.
- [27] T. Furuhashi, T. Makino, Y. Idei, H. Ishigaki, A. Takada, and T. Maki. Morphology and crystallography of precipitates in Ti–Mo binary alloys. *Materials transactions-JIM*, 39:31–39, 1998.
- [28] TW Duerig, GT Terlinde, and JC Williams. Phase transformations and tensile properties of Ti–10V–2Fe–3Al. *Metallurgical and Materials Transactions A*, 11(12):1987–1998, 1980.
- [29] F. Prima, P. Vermaut, G. Texier, D. Ansel, and T. Gloriant. Evidence of α -nanophase heterogeneous nucleation from ω particles in a β -metastable Ti-based alloy by high-resolution electron microscopy. *Scripta materialia*, 54(4):645–648, 2006.
- [30] S. Azimzadeh and H. J. Rack. Phase transformations in Ti–6.8 Mo–4.5 Fe–1.5 Al. *Metallurgical and Materials Transactions A*, 29(10):2455–2467, 1998.

- [31] B. Kokuoz. The role of crystallographic relationships between alpha and beta phases on the elevated temperature isothermal phase transformation kinetics in TIMETAL LCB (Ti–6.5 Mo–4.5 Fe–1.5 Al). Master’s thesis, Clemson University, 2008.
- [32] T. Sakamoto, K. Nakai, M. Maeda, and S. Kobayashi. Variation of hardness with microstructure evolutions in metastable β titanium alloy TIMETAL® LCB. In *Materials Science Forum*, volume 561, pages 2067–2070. Trans Tech Publ, 2007.
- [33] Y. Kosaka, S.P. Fox, K. Faller, and S.H. Reichman. Properties and processing of timetal lcb. *Journal of materials engineering and performance*, 14(6):792–798, 2005.
- [34] J. I. Goldstein, D. E. Newbury, P. Echlin, D. C. Joy, C. E. Lyman, and E. Lifshin. *Scanning electron microscopy and X-ray microanalysis*. Kluwer Academic/Plenum Publish, 2003.
- [35] Wikipedia. Vickers hardness test — wikipedia, the free encyclopedia, 2012. [Online; accessed 28-March-2012].
- [36] B. D. Cullity. *Elements of X-ray Diffraction*. Addison-Wesley, 1956.
- [37] N. W. Ascroft and D. Mermin. *Solid State physics*. Harcourt College Publishing, 1976.
- [38] G. W. Smith. Precipitation kinetics in an air-cooled aluminum alloy: A comparison of scanning and isothermal calorimetry measurement methods. *Thermochimica acta*, 313(1):27–36, 1998.
- [39] G. Höhne, W. Hemminger, and H. J. Flammersheim. *Differential scanning calorimetry*. Springer Verlag, 2003.
- [40] P.L. Rossiter. *The electrical resistivity of metals and alloys*. Cambridge Univ Pr, 1991.
- [41] G. E. Dieter. *Mechanical Metallurgy*. McGraw-Hill Book Company, 1986.
- [42] H. Czichos, T. Saito, L.R. Smith, and L. Smith. *Springer handbook of materials measurement methods*, volume 978. Springer Verlag, 2006.
- [43] T.H. Courtney. *Mechanical behavior of materials*. McGraw-Hill, 1990.
- [44] T. Gloriant, G. Texier, F. Sun, I. Thibon, F. Prima, and J.L. Soubeyrou. Characterization of nanophase precipitation in a metastable β titanium-based alloy by electrical resistivity, dilatometry and neutron diffraction. *Scripta Materialia*, 58(4):271–274, 2008.
- [45] F. Prima, P. Vermaut, D. Ansel, and J. Debuigne. ω precipitation in a beta metastable titanium alloy, resistometric study. *Materials transactions-JIM*, 41(8):1092–1097, 2000.

- [46] M. Ikeda, S. Y. Komatsu, T. Sugimoto, and K. Kamei. Negative temperature dependence of electrical resistivity in Ti–Mo binary alloys. In *Sixth World Conference on Titanium*, pages 313–318, 1988.
- [47] Z. Matej. *Structure of submicrocrystalline materials studied by X-ray diffraction*. PhD thesis, Charles University in Prague, 2011.

List of Tables

3.1	Typical properties of TIMETAL LCB	14
3.2	Chemical composition of TIMETAL LCB	14
3.3	Grain Boundary Alpha Characterization	15
5.1	Microhardness measurement results	30
5.2	Average chemical composition of TIMETAL LCB determined by EDS and its comparison with nominal values	44
5.3	Average chemical composition of grain boundary α phase deter- mined by EDS	46
5.4	Tensile properties – ultimate tensile strength (UTS), elongation, yield stress ($\sigma_{0.2}$) and plastic strain (ε_p)	48

List of Figures

2.1	Unit cells of Ti [4]	3
2.2	Slip planes and directions in the hexagonal α phase [4]	4
2.3	Effect of alloying elements on phase diagrams of titanium alloys [5]	5
2.4	Pseudo-binary section through a β isomorphous phase diagram showing important equilibrium and metastable phases as well as the classification of Ti alloys [4]	7
2.5	Effect of the displacive wave ($k = \frac{2}{3}[111]_{\beta}$) on the bcc lattice of the β phase, producing ω structure [25]	9
2.6	The $\beta \rightarrow \omega$ transformation represented as a displacement wave mechanism. The incomplete (trigonal symmetry) and complete transformation (hexagonal) is shown [6]	9
3.1	The molybdenum equivalent of various β titanium alloys	15
3.2	The tensile test specimen	17
3.3	Vickers microhardness scheme [35]	18
3.4	Scheme of $\theta - 2\theta$ Bragg–Brentano focusing geometry, X-rays from tube T are incident on a crystalline sample C which rotates about the center of the spectrometer O , D is the detector. The tube is fixed, the sample angle varies as θ and the detector angle varies as 2θ [36]	19
3.5	A Bragg reflection from a family of lattice planes with lattice spacing equal to d	20
5.1	The grain structure of an initial state of TIMETAL LCB	25
5.2	The initial state of the material; grain boundary α is shown	26
5.3	The temperature dependence of resistivity at the heating rate of $5\text{ }^{\circ}\text{C}/\text{min}$ (black solid curve) and a corresponding DSC measurement at the same heating rate (grey dashed curve)	28
5.4	The temperature dependence of resistivity at the heating rate of $50\text{ }^{\circ}\text{C}/\text{min}$ (black solid curve) and a corresponding DSC measurement at the same heating rate (grey dashed curve)	28
5.5	Evolution of microhardness with increasing ageing time; condition 1 and 2 aged at $400\text{ }^{\circ}\text{C}$, $450\text{ }^{\circ}\text{C}$ and $500\text{ }^{\circ}\text{C}$ are shown	31
5.6	Microhardness evolution for condition 1 and 2 aged at $400\text{ }^{\circ}\text{C}$	32
5.7	Microhardness evolution for condition 1 and 2 aged at $450\text{ }^{\circ}\text{C}$	32
5.8	Microhardness evolution for condition 1 and 2 aged at $500\text{ }^{\circ}\text{C}$	33
5.9	Volume fractions of α , β and ω phases in samples aged at $400\text{ }^{\circ}\text{C}$	35
5.10	Volume fractions of α , β and ω phases in samples aged at $450\text{ }^{\circ}\text{C}$	35
5.11	Volume fractions of α and β phases in samples aged at $500\text{ }^{\circ}\text{C}$	36
5.12	Influence of ageing time and temperature on lattice parameters of α , β and ω phase	37
5.12	(Continued) Influence of ageing time and temperature on lattice parameters of α , β and ω phase	38
5.12	(Continued) Influence of ageing time and temperature on lattice parameters of α , β and ω phase	39

5.13	Condition 1, aged at 400 °C for 0.5 h	40
5.14	Condition 2, aged at 400 °C for 0.5 h	40
5.15	Condition 1, aged at 400 °C for 4 h	40
5.16	Condition 2, aged at 400 °C for 4 h	40
5.17	Condition 1, aged at 400 °C for 32 h	40
5.18	Condition 2, aged at 400 °C for 32 h	40
5.19	Condition 1, aged at 400 °C for 256 h	41
5.20	Condition 2, aged at 400 °C for 256 h	41
5.21	Condition 1, aged at 450 °C for 0.5 h	43
5.22	Condition 2, aged at 450 °C for 0.5 h	43
5.23	Condition 1, aged at 450 °C for 4 h	43
5.24	Condition 2, aged at 450 °C for 4 h	43
5.25	Condition 1, aged at 450 °C for 32 h	43
5.26	Condition 2, aged at 450 °C for 32 h	43
5.27	Condition 1, aged at 450 °C for 256 h	44
5.28	Condition 2, aged at 450 °C for 256 h	44
5.29	Condition 1, aged at 500 °C for 0.5 h	45
5.30	Condition 2, aged at 500 °C for 0.5 h	45
5.31	Condition 1, aged at 500 °C for 4 h	45
5.32	Condition 2, aged at 500 °C for 4 h	45
5.33	Condition 1, aged at 500 °C for 32 h	45
5.34	Condition 2, aged at 500 °C for 32 h	45
5.35	Condition 1, aged at 500 °C for 256 h	46
5.36	Condition 2, aged at 500 °C for 256 h	46
5.37	EDS spectrum taken from a larger area of the sample	47
5.38	EDS spectrum of grain boundary α phase	47